



UNIVERSITEIT VAN AMSTERDAM



MSc Physics and Astronomy

Advanced Matter and Energy Physics

Master Thesis

Study of Ultrafast Laser-Induced Acoustic with Plasmonics Gratings Using Pump-Probe Measurements

by

Jeffrey SUEN Yat Wang

14355868

Supervisors: Prof. dr. Paul Planken
ir. Thomas van den Hooven
Date: Sept 20, 2024
Credits & Period: 60 ECTS, Oct 2023 - Sept 2024

Abstract

Ultrafast laser-induced strain waves offer a proposed technique for detecting buried gratings which is important in the microchip manufacturing process. However, the optical detection signal strength is not sufficient for industrial applications. This thesis explores the plasmonic enhancement of photoacoustic signals generated by ultrashort laser pulses on a 130 nm thick aluminum layer deposited on a silicon wafer with an etched grating. A femtosecond pump-probe system was employed to detect time-resolved reflection and diffraction changes induced by intense laser pulses launching ultrasonic waves into an opaque material aluminium. The surface plasmon polariton (SPP) resonance was investigated with two methods: First, we used a fixed probe wavelength and varied the angle of incidence. Second, the angle of incidence is fixed and the reflection change per wavelength is measured for a broad range of wavelengths, using a spectrometer.

Reflection change measurements with narrow band probe laser pulses at varying angle of incidence shows time-dependent oscillations around the SPP resonance angle, but the sources of the measured oscillations are unknown. Also, the measured time-dependent changes could not be attributed to the expected longitudinal waves according to the calculated round trip time. Reflection change measurements at a fixed angle of incidence with white light continuum probe pulses also show no clear evidence of longitudinal wave echoes, but they show similar features found in the angle-dependent measurements. This study illustrates the connection between varying the angle of incidence and varying the probe wavelength around the SPP resonance configuration.

Analysis of the acoustic properties of the materials suggests that the absence of clear strain wave reflections may result from the small acoustic impedance mismatch between the aluminium layer and the silicon substrate, which limits the strain wave amplitude reflection coefficient to only around 6% at the interface. The aluminum layer deposited may also be porous, not ideal for efficient propagation of acoustic waves. This study concludes by highlighting the importance for improved choice of

materials for future investigations of laser-induced photoacoustic signals, especially the acoustic impedance mismatch at an interface.

Contents

Abstract	i
1 Introduction	1
2 Theory	3
2.1 Two-Temperature Model	3
2.2 Photoacoustics	5
2.3 Surface Plasmon Polaritons	7
3 Experimental methods	11
3.1 Overview	11
3.2 Pump-Probe	12
3.3 Ultrafast laser	15
3.4 Sample characterization	16
3.4.1 Surface structure	16
3.4.2 White light spectroscopy	17
3.5 Transient grating	21
4 Results	23
4.1 Overview	23
4.2 Transient grating diffraction changes	23
4.3 Grating reflection changes	26
4.3.1 Single wavelength probe	26
4.3.2 White light probe	32
4.4 Acoustic impedance mismatch	39
5 Conclusion	41
References	44

A	First appendix	46
A.1	Laser peak fluence	46

1

Introduction

Every year, the performance of computer chips is increasing. The main method to enhance microchip performance is to increase the density of transistors in integrated circuits. In order to improve, features printed on a microchip need to be smaller. Recently, IBM's technology produced chips with features of 2-nanometer size. There are 50 billion transistors on a microchip no larger than a fingernail [1]. These microchip designs are pushing the limit to how small printed structures can be.

During the nanolithography manufacture processes of stacked microchips, such as the 3D-NAND flash memory chips in modern solid state drives, structures are printed layer by layer. To ensure different layers are connected correctly, the alignment of the wafer at each lithography step needs to be accurate. Alignment gratings are printed onto the silicon wafer such that its position can be precisely measured with the diffraction of laser beams. However, during the etching processes, opaque masking layers are deposited on top of the gratings. This makes direct diffraction measurements difficult. [2]

Ultrafast optical pulses are capable of generating strain waves within materials, serving as a potentially useful technique for detecting buried grating with strain waves. In recent decades, significant progress has been made in understanding the creation and propagation of these laser-induced strain waves. These waves have also been utilized to investigate various physical phenomena and material properties, such as the electronic structure of materials and surface deformation.

Typically, we detect these strain waves by measuring changes in optical properties via the reflectance and transmittance of a surface or interface. These strain waves can also be observed by measuring light diffracted off a strain-wave-induced grating. However, optical reflectance changes caused by strain waves are relatively small and difficult to detect. They require complex experimental setups involving sophisticated signal modulation techniques to improve the signal-to-noise ratio in measurements. Therefore, it is crucial to develop methods to enhance these signals. One promising approach involves exploiting surface plasmonic resonances.

Surface plasmon polaritons (SPPs) are collective oscillations of electrons in the metal that couple with electromagnetic waves propagating along a metal-dielectric interface. They can be excited using various techniques, including the Kretschmann geometry [3] and plasmonic gratings [4]. For instance, plasmonic gratings have been employed to study strain waves within acoustic cavities [5] and to detect strain waves in gold layers [5]. It is shown that the optical changes by strain waves can be enhanced using SPPs [6].

When surfaces with structures, such as a grating, are exposed to ultrashort laser pulses, additional strain waves, such as surface acoustic waves (SAWs) and particle-like normal modes (NMs), may be generated. The influence of these additional acoustic waves on the grating surface plasmon polariton resonance is not yet fully understood.

The goal of this thesis is to study laser-induced photoacoustics in a 130 nm aluminium grating and the effects of surface plasmon polaritons on the detection of acoustic waves. In Chapter 2, we provide the theoretical background to the major concepts used as the basis for this study. We introduce the two-temperature model, the generation of laser-induced strain waves and their propagation, and surface plasmon polaritons. In Chapter 3, we describe the experimental setup and explain the experiments performed. In Chapter 4, we present the experimental data and discuss the measurement results. Finally, we summarize this thesis into a conclusion in Chapter 5.

2

Theory

2.1. Two-Temperature Model

When a metal surface is irradiated by an ultrafast laser pulse, the energy from the laser is initially absorbed by the free electrons in the metal. For an optically thick layer, the intensity of the incident laser pulse would exponentially decay into the metal layer. Assuming the penetration depth of the laser light is significantly shorter than the thickness of the layer, the reflection of the laser light from the material/substrate interface is not considered. Then, the intensity of the laser light can be described by a function of the depth z from the surface into the metal,

$$I(z) = (1 - R)I_0 e^{-z/d_p} \quad (2.1)$$

where I_0 is the initial laser intensity at the surface, R is the power reflection coefficient of the metal and d_p is the penetration depth of the laser light into the metal. The energy of the laser pulse is absorbed by the free-electron gas in the metal layer. The heat then diffuses within the electron gas while simultaneously being transferred to the lattice. For long pulses or continuous-wave lasers, this process happens on a few picosecond timescale. The electrons transfer their energy to the lattice that heats up, with the two systems in equilibrium. With intense pulses, or shorter pulses, the two systems are not in equilibrium instantaneously after illumination.

In a non-equilibrium situation upon rapid absorption of energy from the laser pulse,

the electron gas and the lattice initially have different temperatures. After the initial rise in temperature of the electron gas, the energy is gradually transferred to the lattice. For long pulses, the absorbed heat in the free electrons is transferred to the lattice relatively quickly. However, after an ultrafast laser pulse which ends before equilibrium is reached, the heat transfer dynamics between the electron gas and the lattice becomes evident. The Two-Temperature Model (TTM) can be used to describe the dynamics of this non-equilibrium heating or cooling process [7].

The TTM separates the system of electrons and the lattice, each with its own temperature. The system can be characterized by a pair of coupled differential equations: one heat equation for the electron temperature $T_e(z, t)$ and another heat equation for the lattice temperature $T_l(z, t)$, both as a function of depth z and time t . [7] In one dimension, in the depth of the material, the time-dependent heat equations can be written as

$$C_e(T_e) \frac{\partial T_e}{\partial t} = \frac{\partial}{\partial z} (k_e(T_e, T_l)) - g(T_e - T_l) + \alpha I(z, t), \quad (2.2)$$

$$C_l \frac{\partial T_l}{\partial t} = g(T_e - T_l), \quad (2.3)$$

where C_e and C_l are the heat capacities of the electrons and lattice respectively, $k_e(T_e, T_l)$ is the electron thermal conductivity which can be a function of the temperatures, g is the electron-phonon coupling constant, and α is the inverse of the optical penetration depth. The electron-phonon coupling constant g determines the energy transfer rate between the two subsystems, which is an intrinsic property of the material.

In the equations, the heat capacities are multiplied by the derivatives of temperatures with respect to time. This represents the change in energy in each system, in power per unit volume. In Eqs. (2.2), on the right-hand side, the first term describes the diffusion deeper into the layer, where heat diffusion by the lattice via phonons is neglected. The second term represents thermal loss by energy transfer to the lattice due to electron-phonon coupling. The third term represents the source of the deposited laser energy. The energy of the laser pulse is turned into heating of the electron gas.

The rise in lattice temperature is accompanied by the generation of thermal stress, as the layer "wants" to expand, leading to a time-dependent stress that launches strain waves travelling through the material.

Different temperature distributions can be obtained from the two-temperature model with different material characteristics. The rate of energy transfer between the two systems and the resulting temperature distribution are heavily influenced by both the electron-phonon coupling constant g and the thermal conductivity of the electron gas k_e .

The TTM only works when the electrons have thermalised. The time it takes after the absorption of a laser pulse depends on material parameters, but is typically in the range of a few hundred femtoseconds [8]. The model is thus useful for describing the temperature evolution after the initial peak, when the electron-electron scattering has thermalized the electron gas. Here, this model is used assuming that lateral thermal dissipation due to temperature gradient within the plane of the target surface is negligible, which is arguably true when the irradiated area is much larger than the depth of material in question.

2.2. Photoacoustics

The thermal stress σ_{th} in the direction z normal to the metal surface induced by the lattice temperature change ΔT_l can be expressed as, [9]

$$\sigma_{th}(z, t) = -3B\beta\Delta T_l(z, t) \quad (2.4)$$

where B is the bulk modulus of the metal and β is the coefficient of linear thermal expansion. When an ultrafast laser pulse hits the surface of the metal, heat is transferred into the metal, inducing thermal stress. Depending on the electron-phonon coupling constant g and the thermal conductivity of the electron gas k_e of the material, the stress will be either localised or homogeneously distributed. The time-dependent shapes of the generated strain wave will therefore also be different.

A strong electron-phonon coupling with a low electron gas thermal conductivity would lead to a quick transfer of heat from the electrons to the lattice. The lattice temperature near the surface where the laser energy was absorbed increases rapidly before the heat diffuses deeper into the material through the electrons, resulting in steep temperature gradients more or less following the absorption profile of the light [10]. Thus, the heating is localized near the surface within the first few picoseconds.

In this case, a more compact traveling longitudinal acoustic wave packet would be

launched, localized in time but containing a broad range of acoustic frequencies. In a thin layer, the wave could be reflected back from the opposite surface and reflected again on the top surface multiple times as "echoes". This also depends on the properties of the metal boundary interfaces. These echoes can translate into periodic changes in optical properties at the surface which can be detected via another probe laser pulse.

Conversely, a weak electron-phonon coupling constant with a high electron gas thermal conductivity would lead to a more gradual energy transfer to the lattice, whereas the hot electrons are allowed to spread their energy deeper into the material, making the resulting temperature distribution on the lattice more uniform. In this case, the thermal stress is more gradual. A standing strain wave forms like a breathing mode, given that boundaries reflect the acoustic waves.

Then, following the derivation by Thomsen et. al. [9] and de Haan et. al. [2], we have the equations of elasticity in the z-direction,

$$s_z(z, t) = \frac{\partial u(z, t)}{\partial z}, \quad (2.5)$$

$$\begin{aligned} \sigma_z(z, t) &= \sigma_{str} + \sigma_{th} \\ &= (\lambda + 2\mu)s_z(z, t) - 3B\beta\Delta T_l(z, t), \end{aligned} \quad (2.6)$$

$$\rho \frac{\partial^2 u(z, t)}{\partial t^2} = \frac{\partial \sigma_z(z, t)}{\partial z}, \quad (2.7)$$

where s_z is the strain, u is the displacement, σ_z is the sum of the stress resulting from the elastic strain σ_{str} and from thermal expansion σ_{th} , λ and μ are the Lamé parameters, and ρ is the density of the material. Eq. (2.5) defines the strain in the z-direction, normal to the surface of the sample, Eq. (2.6) describes the total stress in the material, and Eq. (2.7) is the equation of motion of a volume element in the sample material by Newton's second law. From these equations, we find that thermal expansion of the material leads to strain, which generates stress with a term proportional to the strain and the lattice temperature change. These stress can propagate through the material resulting in a longitudinal strain wave.

Not only can a laser beam generate longitudinal acoustic waves in the z-direction of the material, acoustic waves parallel to the layer can also be excited given that a periodic structure exists on the surface, since the thermal stress created by the laser beam would inherit this periodicity. These acoustic waves traveling along the surface

are commonly known as a surface acoustic wave (SAW). They are probably Rayleigh waves [2], which have transverse and longitudinal components, because the direction of thermal expansion can be parallel or perpendicular to the surface. The spatial periodicity of the SAWs would most likely also be the same as that of the surface structure.

2.3. Surface Plasmon Polaritons

Surface plasmon polaritons (SPPs) are electromagnetic waves that travel along the interface between a dielectric and a metal. These waves are coupled oscillations of the electromagnetic field and oscillations of the electron gas in the metal, resulting in a surface-bound mode. A schematic diagram of an SPP is shown in Fig. 2.1.

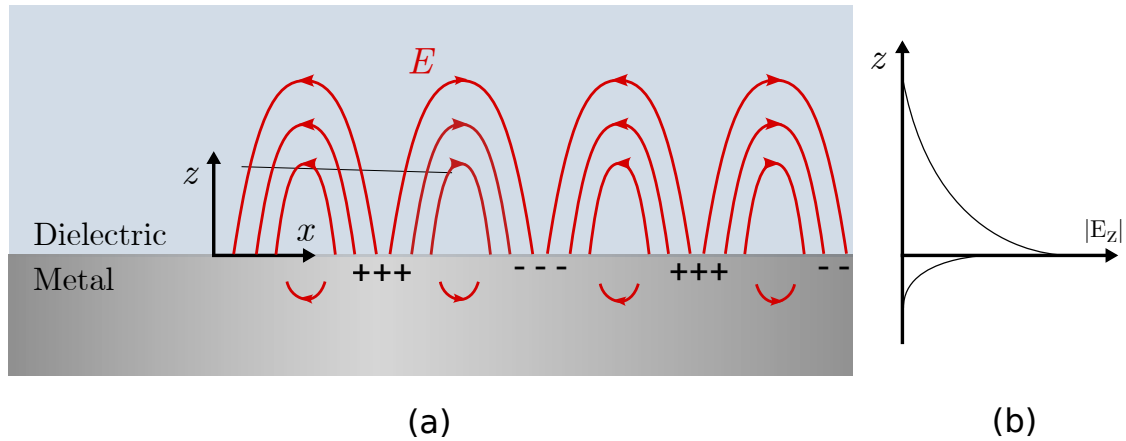


Figure 2.1: (a) A schematic diagram of the electric fields and surface charges of an SPP excited at the dielectric/metal interface. (b) The evanescent electric fields decaying exponentially in the direction perpendicular to the interface, both into the metal and the dielectric.

The electromagnetic field in the direction perpendicular to the surface (as shown in Fig. 2.1 b) associated with SPPs decays exponentially in the direction perpendicular to the interface, both into the metal and the dielectric. There is also an x -component in the direction of propagation along the interface. Because the electromagnetic wave is coupled to surface charge density oscillations, SPPs have a wave vector different from light at the same frequency in vacuum. The dispersion relation of SPPs is related to the dielectric function of the metal and dielectric. The SPP propagation constant

k_{SPP} is given by, [4]

$$k_{SPP} = \frac{\omega}{c} \sqrt{\frac{\epsilon_m \epsilon_d}{\epsilon_m + \epsilon_d}}, \quad (2.8)$$

where ω is the angular frequency of the incident electromagnetic wave, ϵ_m and ϵ_d are the dielectric functions of the metal and the dielectric respectively, and c is the speed of light. To simplify, we only consider the real part of the complex dielectric functions, neglecting attenuation.

The real part of the dielectric function of most metals is below -1 and the dielectric function of air is approximately 1. An SPP can only be excited if the real part of the dielectric function of the metal is smaller than -1. Applying the dielectric functions $\epsilon_m < -1$ and $\epsilon_d = 1$ to Eq. (2.8), we find that $k_{SPP} > k_0 = \omega/c$. Hence, SPPs have a wavelength shorter than light at the same frequency, which also means higher momentum. Further analysis of the z-component of the k-vector shows that, for dielectrics with $\epsilon_d \neq 1$, a bound SPP mode exists only if $\epsilon_m < -\epsilon_d$ for a metal-dielectric interface. A schematic plot of the dispersion relation of k_{SPP} for a typical metal is shown in Fig. 2.2.

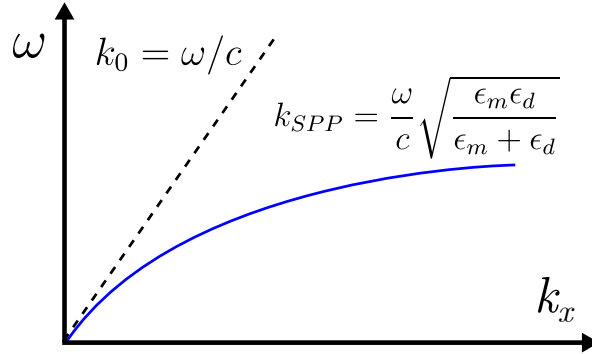


Figure 2.2: Schematic plot of the dispersion relation of k_{SPP} for a typical metal. For a certain frequency ω , k_{SPP} is always larger than the wave vector k_0 of light of that frequency in vacuum.

Since the free-space photon does not have the same k-number as the corresponding SPP of the same frequency, it is impossible to excite an SPP simply by shining light onto the metal surface from air.

One way of coupling photons into SPPs at the surface is with a grating. The component of the wave vector parallel to the surface can be increased or decreased by an amount related to the period of the grating. We consider a k -vector intrinsic to the periodicity

of the grating. It is denoted as $k_g = 2\pi/\Lambda$, where Λ is the grating period. By adding or subtracting multiples of k_g , the grating harmonics provide pseudo-momentum in addition to the incident light such that the combined wave vector can match the SPP. A grating can couple light to SPPs if the following equality is satisfied [11].

$$\begin{aligned} |k_x \pm Nk_g| &= k_{SPP} \\ \left| \frac{\omega}{c} \sin \theta \pm N \frac{2\pi}{\Lambda} \right| &= \frac{\omega}{c} \sqrt{\frac{\epsilon_m \epsilon_d}{\epsilon_m + \epsilon_d}} \end{aligned} \quad (2.9)$$

$k_x = (\omega/c) \sin \theta$ is the x-component of the wave vector of the incident light in vacuum where θ is the angle of incidence, and N is an integer. Since the grating k-vector can be added or subtracted, and only the magnitudes between the left and right-hand side of Eq. (2.9) need to match, it is possible that the SPP launched is in the opposite direction to k_x , given the right wavelength of light and angle of incidence. Note that only p-polarized light can excite an SPP since the component of the electric field normal to the surface is required to drive the transverse oscillation of charge density at the metal-dielectric interface.

The derivation of the SPP propagation constant k_{SPP} in Eq. (2.8) is based on a flat metal-dielectric interface. This becomes an approximation in Eq. (2.9) for a grating when we simply added the grating k-vector k_g while still using the same equation for k_{SPP} . The assumption will be more inaccurate if the grating amplitude is larger, deviating from a flat surface.

As a result of the resonance conditions of SPPs, they are highly sensitive to changes in the properties of the metal near the surface, making them useful in sensing applications.

The SPP resonance wavelength of a sample at a certain incident angle can be identified by measuring the reflectance spectrum with a spectrometer. When coupling to an SPP, some energy from the incident light turns into energy in the SPP. Therefore, the energy in the reflection would decrease accordingly near the SPP resonance wavelength.

Minute changes in the optical properties of the metal can shift the resonance wavelength. Thus, precise measurement of reflectance changes near a SPP resonance can reveal dynamics on a surface. The resonance conditions of an SPP are shown to be sensitive to variations in the dielectric function of the metal, which depends

on the electron density. When a longitudinal acoustic wave reaches the surface, the expansion and contraction causes oscillations in electron density, as the longitudinal waves are density waves, thus modulating the SPP resonance wavelength. The reflectance of light near the resonance frequency would change more rapidly under small perturbations to the electron density. The reflectance of wavelengths at the slopes on the sides of the SPP resonance in the reflectivity spectrum of the material changes the most when the resonance wavelength shifts. Therefore, we expect the corresponding oscillation amplitudes to be the strongest at the probe laser wavelengths slightly shorter or higher than at the resonance wavelength, rather than probing at resonance [2].

3

Experimental methods

3.1. Overview

This chapter describes the pump-probe experiments performed, the lasers used and characterization of the sample. We perform experiments with ultrafast laser-induced photoacoustics on a thin aluminium layer on a silicon wafer as the sample target. An area in the center of the wafer is etched with a grating.

A pump laser pulse with a fixed wavelength illuminates the etched grating part of the sample. The probe laser is incident on the same spot at and around the SPP resonance angle. The intensity of the reflected light is measured.

The probe laser is then changed from a single central wavelength pulse into a white light continuum, with wavelengths ranging from 600 nm to around 900 nm, at a fixed angle of incidence. The reflected light is then measured with a spectrometer, such that the reflection change in a range of wavelengths is measured.

In a different experiment, the pump laser pulse is split into two arms to create a transient grating on a flat part of the sample. The probe laser illuminates the same area and light is diffracted by the transient grating. The intensity of the diffracted light is measured as the pump-probe delay is varied. Thus, the diffraction change caused by the pump laser is observed.

3.2. Pump-Probe

The primary experimental approach employed in this thesis is the pump-probe technique. A short laser pulse, the *pump*, excites the sample, inducing optical changes, while a second, delayed pulse, the *probe*, measures the resulting changes in the material, such as reflectance or diffraction efficiency. By varying the time delay between the pump and probe pulses, the time-dependent evolution of the pump-induced changes can be observed.

A schematic illustration of the setup is shown in Figure 3.1. The setup includes a high-intensity pump pulse directed through a rotating chopper installed in the beam path synchronized with the pulse train blocking every other shot of the pump. This halves the output repetition rate to 500 Hz. The pump pulses are focused onto the sample via a lens of focal length 20 cm. An optical delay line in the beam path of the pump pulse controls the relative time delay between the pump and probe pulses to sub-picosecond precision by changing the path length.

The pump-induced changes are subsequently analyzed using a weaker probe pulse. The path length is adjusted in a way that the pump and probe pulse arrive at the sample at nearly the same time. The probe beam is split into two by a beam splitter, where one of them is measured as a reference, and the other is measured after reflection or diffraction from the sample.

During the experiment, for every two consecutive probe pulses that arrive at the sample, only one is affected by the changes induced by the pump pulse, since every other pump pulse is blocked by the chopper. The probe pulses that encounter these pump-induced changes are termed "pumped shots" (*), while those where the pump beam is blocked by the chopper are called "blocked shots" (0). With these measurements, we can calculate the pump-induced relative reflection changes by

$$\frac{\Delta R}{R} = \frac{I^* - I^0}{I^0}, \quad (3.1)$$

where I^* and I^0 are the detected intensities of the pumped and the blocked shots respectively, and R would be the reflection from the sample.

Each of the probe laser pulses is split by a beam splitter into one that is reflected by the sample, and another one that goes to a reference detector without hitting

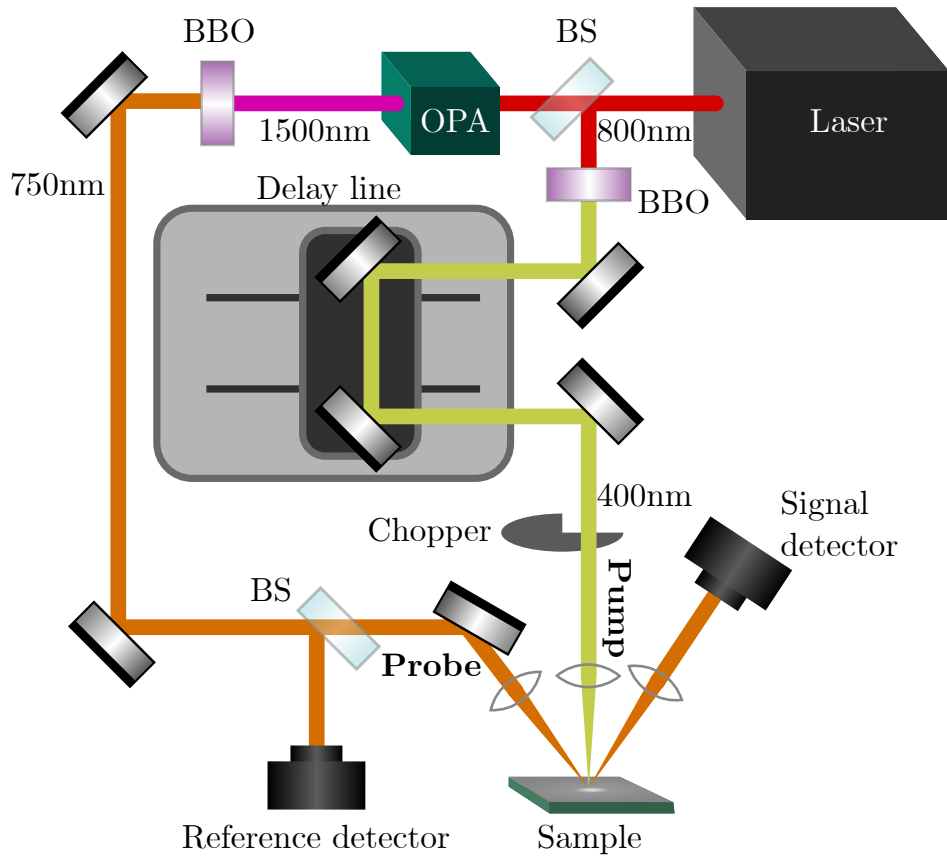


Figure 3.1: Schematic of pump-probe measurement setup.

the sample. Every pumped and blocked shot is normalized against the reference to compensate for any fluctuation of the probe pulse energy not caused by the sample. The reflection change is measured 2000 times for each time delay and averaged. The average relative changes normalized with reference pulses are calculated by

$$\frac{\Delta R}{R} = \left\langle \frac{I^*/I_{ref}^* - I^0/I_{ref}^0}{I^0/I_{ref}^0} \right\rangle. \quad (3.2)$$

Alternatively, the absolute difference can also be calculated in case the blocked signal is near zero. Likewise, to normalize the difference and make them more comparable, the blocked shot is scaled by the ratio between the reference intensity of the pumped

shot and the blocked shot. The absolute difference is calculated by

$$\Delta\eta = \left\langle I^* - I^0 \left(\frac{I_{ref}^*}{I_{ref}^0} \right) \right\rangle. \quad (3.3)$$

where $\Delta\eta$ can be the diffraction or reflection change depending on the setup.

These techniques enables the measurement of the pump pulse's impact on the sample at various times following its excitation. With many consecutive measurements varied by small delay increments, we can obtain a time-dependent trace of the change.

In the white light probe measurements, the setup is altered such that a white light continuum is generated instead of the 750 nm probe laser. The generated white light pulses are guided to be incident onto the sample at the SPP resonance angle for a wavelength of 750 nm. To capture the pump-induced reflection changes induced on a wide spectrum of light, a spectrometer is used as the detector.

The spectrometer consists of a diffraction grating to spread the wavelengths from the white light horizontally, and a scientific CMOS camera (Zyla, Andor) for intensity measurement. The sensor readout is split into two rectangular strips of pixels. One measures the sample signal, and the other measures the reference. Diffracted light of the signal and the reference from the grating is aligned horizontally onto each strip such that every column of pixels detects one wavelength. Signals from the pixels are averaged along each column within each strip.

Before the measurement, the spectrometer needs to be calibrated to match the pixels to their corresponding wavelengths. A didymium glass filter is used as a reference material for its strong absorption peaks within the spectral range. The original white light is measured on the spectrometer detector. Then, another measurement is done with the same white light passing through the reference material. From these two sets of measurements, the absorbance or optical density (OD) of the reference material is calculated for every pixel column,

$$OD = -\log \left(\frac{I_{rm} - I_D}{I_{cl} - I_D} \right) \quad (3.4)$$

where I_{rm} and I_{cl} are the intensities with and without passing through the reference material, respectively, and I_D is the dark background intensity without white light.

We obtain the absorbance of the reference material at every pixel. By matching the peaks measured with the peaks in the given absorption spectrum of the reference material, a wavelength can be mapped onto each pixel.

To eliminate any horizontal shift discrepancy between the signal and reference strips, further lateral shifting is done in software to minimize the total mean square difference in intensity between the two rows of pixels for a given spectrum. In that case both of the strips are properly calibrated.

3.3. Ultrafast laser

In the experiments performed in this thesis, a Ti:Sapphire amplified laser system (Astrella, Coherent) is used as the laser source. This system generates a 1 kHz pulse train, with wavelength centered at 800 nm and a pulse length of 35 fs. Inside the system, an oscillator generates a pulse train of wavelength centered at 800 nm and a pulse length of 35 fs, with a repetition rate of 80 MHz and average power of 450 mW. Out of the pulse train, pulses are selected for further amplification, reducing the repetition rate to 1 kHz. The laser pulses are then stretched by a grating stretcher before passing through a Ti:Sapphire crystal pumped by a Nd:YAG laser, amplifying the pulses. The amplified laser pulses are then compressed by a grating compressor which outputs the 800 nm, 35 fs long pulses at 1 kHz, with an average power of 6 W.

With the 800 nm laser pulses, frequency-doubling is done with a β -Barium borate (BBO) crystal to produce the desired pump laser pulses at 400 nm. A $\lambda/2$ waveplate rotates the polarization of the 800 nm light. Only the horizontal projection of the 800 nm light is frequency-doubled by the BBO crystal.

A portion of the power of the laser pulses from the Astrella system powers an Optical Parametric Amplifier (OPA) system (HE-TOPAS, Light Conversion). This device turns the 800 nm laser pulses into tunable wavelength pulses in the range of 1150 nm to 2400 nm with a pulse length of about 40 fs. These pulses are then frequency-doubled to produce the probe laser pulses used for the detection.

In the white light reflection experiment, white light pulses are used as the probe laser in order to measure the pump-induced reflectance changes in a large wavelength interval. The white light pulses are generated by focusing 1300 nm pulses from the OPA system in a Sapphire crystal. It is a material with third order non-linear optical

properties where several third-order processes, such as self-phase modulation and self-focusing, occur to light of high intensity, resulting in the spectral broadening.

3.4. Sample characterization

3.4.1. Surface structure

The sample used is a silicon wafer featuring an etched grating at its center, with a 130 nm thick aluminium layer deposited on the top surface by e-beam physical vapour deposition (EBPVD). The grating period, also known as the pitch Λ , is 1.6 μm and the grating lines are 100 nm tall.

After the deposition process, an opaque aluminium layer covers the silicon surface with the grating. Since the aluminium layer is thin, it follows the topography of the Si grating, such that the top surface structure also resembles the grating underneath. To get information about the height distribution of the topography of the resulting surface, we use atomic force microscopy to obtain a 3D image, where we can accurately measure the dimensions of the grating lines and inspect the surface of the aluminium.

Atomic Force Microscopy (AFM) is a high-resolution imaging technique that provides detailed topographical data of a surface at the nanometer scale. It operates by scanning a sharp probe, typically a horizontal cantilever with a nanometer-scale tip, across the surface of the sample. As the tip interacts with the surface, it experiences forces such as Van der Waals forces or other electrostatic forces depending on the sample's material properties. These forces cause the sharp tip to be repulsed and the cantilever bends. The deflections are generally measured by a laser beam reflected off the back of the cantilever. By maintaining a constant force between the tip and the sample surface, the AFM can map out the surface contours with exceptional precision, provided that the tip is sharper than the surface feature we would like to observe.

From the resulting data, a 3D surface topography image can be generated, revealing surface features such as the exact shape and dimension of the sample grating and surface roughness. In Fig 3.2, we show the AFM images of a 850 by 850 nm area in the grating part of our sample. From these images, we measure that after Al deposition, the pitch Λ of the grating is about 1600 nm, the grating amplitude is about 100 nm and the line width W is close to 900 nm. This makes the duty cycle approximately 56%.

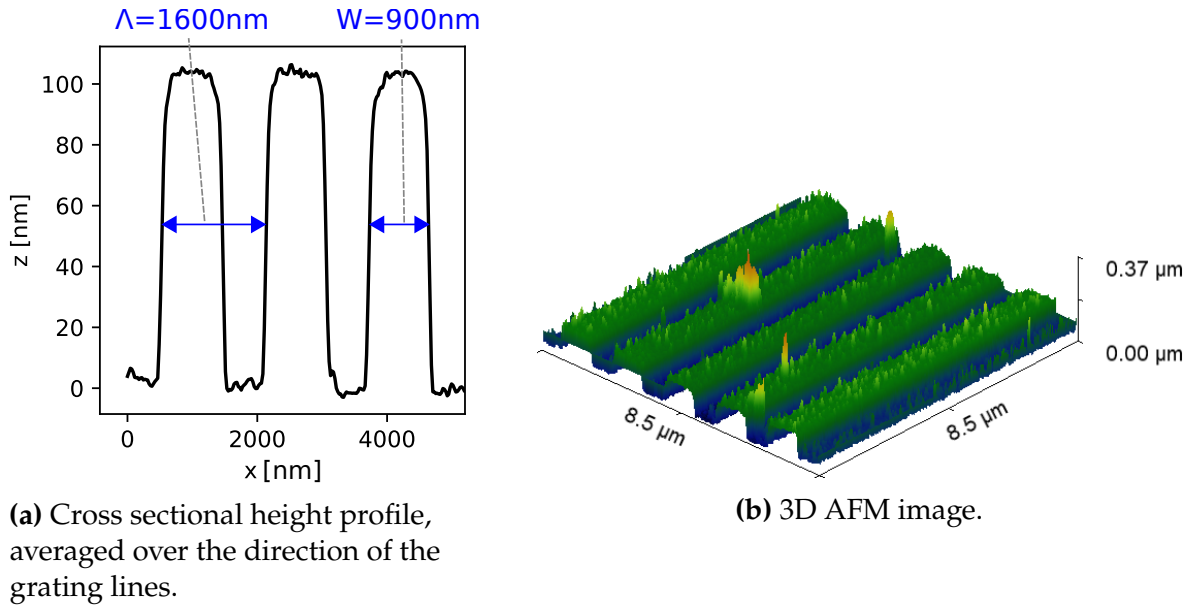


Figure 3.2: AFM images of the 130 nm Al layer deposited on silicon grating.

3.4.2. White light spectroscopy

White light spectroscopy was performed in order to obtain the reflection spectra of our sample. In Fig. 3.3, a schematic depiction of the spectroscopy setup is shown. A halogen light source generates a beam of randomly polarized continuous white light in the range of around 400-1000 nm. The light goes through a polarizer and is focused onto the sample. The light reflects off the sample and is focused into the receiving optical fibre of the spectrometer.

The measurement is done using both s- and p-polarized light selected with the polarizer. We recalled that only when the polarization of the incident light is parallel to the grating lines, SPPs cannot be excited, since the z -component of the electric field is required to drive the oscillation of charge densities. Therefore, only p-polarized light excites SPPs. The sample is laterally translated to measure both the reflection on the flat part, and on the grating part of the aluminium surface. The light is incident on the sample at an angle such that the x -component of the wave vector of the light is perpendicular to the grating lines. We are mainly interested in incident angles where 650-750 nm light would be at the SPP resonance. A range of incidence angles from 31° to 43° is used. Every measurement is repeated for each angle at 1° increments in this range.

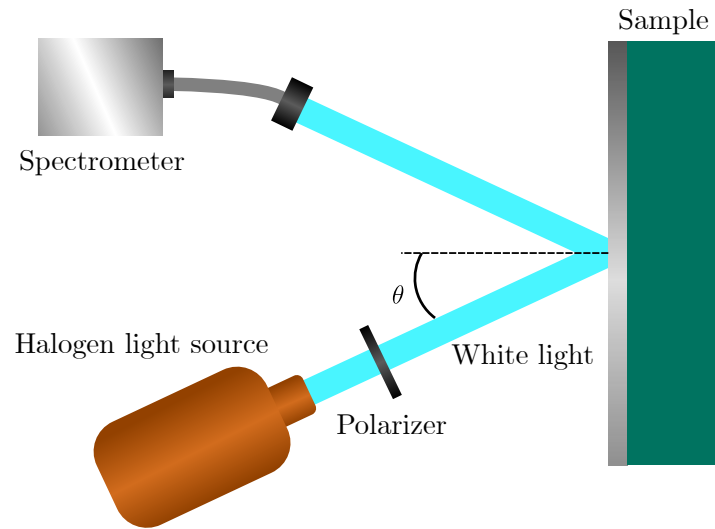


Figure 3.3: Schematic depiction of the white light spectroscopy setup.

With the measured reflection intensities we can calculate the ratio between reflection from the grating and the flat part of the sample. The ratio measured at each angle is plotted in Fig. 3.4. The reflection intensity decreases, moving from the grating to the flat surface at each angle as a result of diffraction by the grating, a difference in absorption, and coupling to SPPs.

Moreover, we can calculate the ratio between the reflection intensity on the grating with p- and s-polarized light. This ratio for each angle is shown in Fig. 3.5. The normal component of the electric field is the part driving the charge density oscillation at the metal-dielectric interface. Therefore, only p-polarized light can excite SPPs, thus the comparison between the reflectance spectra for s- and p-polarized light. Although both p- and s-polarized light are diffracted by the same grating, the diffraction efficiency can be enhanced by excitation of SPPs [12] when the light is p-polarized. This would further decrease the reflection intensities near the SPP resonance. Note that comparing the reflection intensity between p- and s-polarized light gives a better contrast of SPP coupling than simply comparing the reflection from the grating part and the flat part of the sample. We observe that the minimum at around 640 nm incident at 43° , which we attribute to the SPP resonance wavelength, gradually increases in wavelength as the angle of incidence increases, until it seemingly disappears when approaching the other minimum near 880 nm incident at 31° .

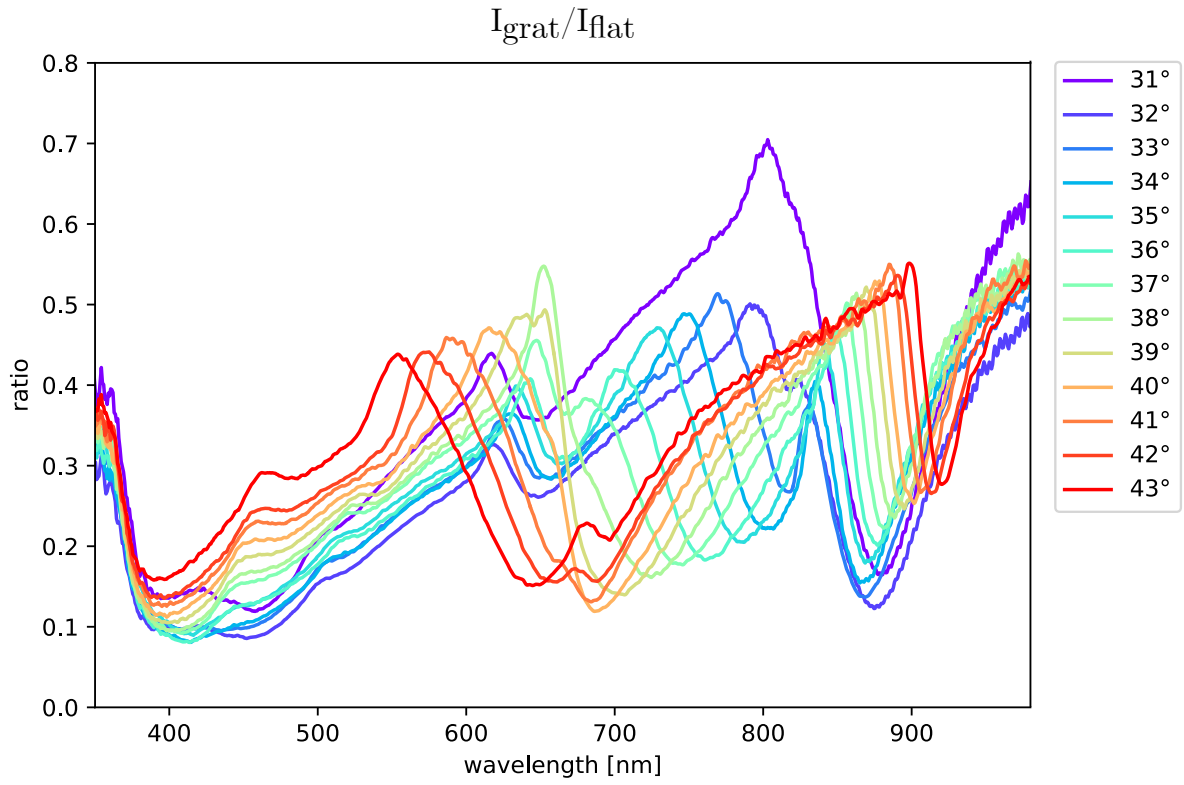


Figure 3.4: Ratio between reflection from the grating part and the flat part of the aluminium surface at various angles with p-polarized light.

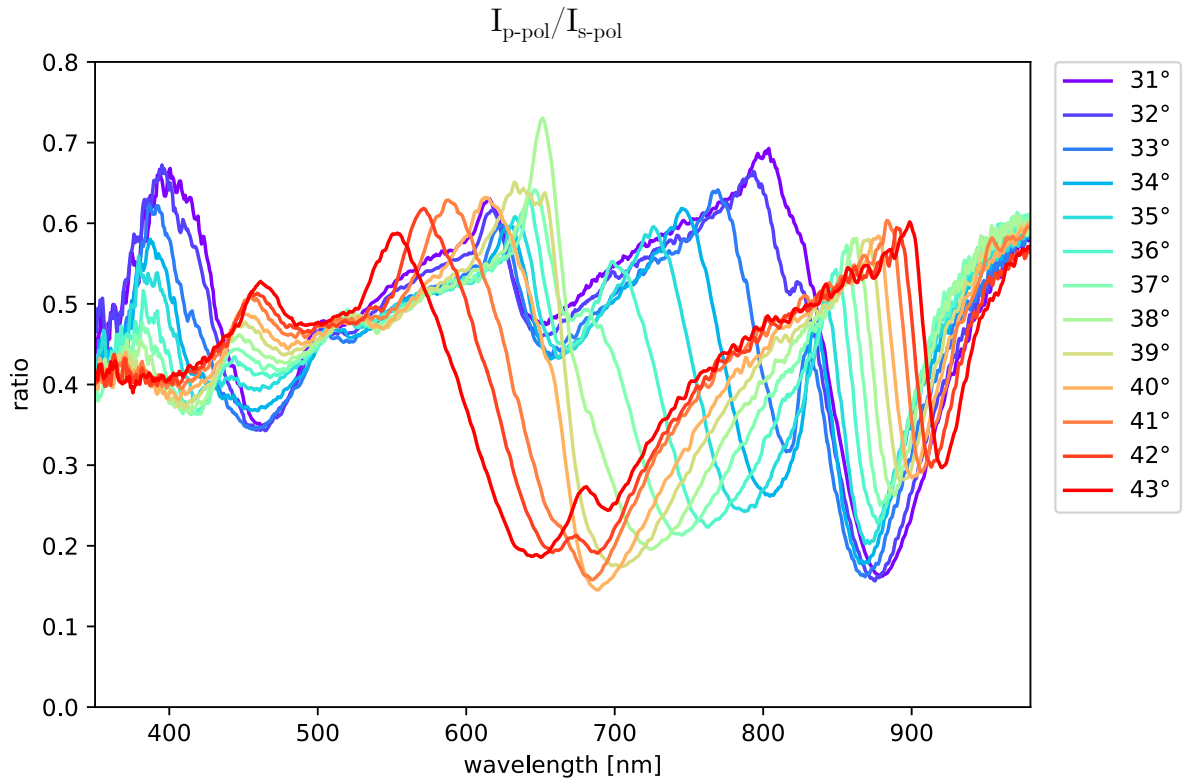


Figure 3.5: Ratio of reflection from the grating part between p- and s-polarized light.

The reflection intensity ratio at a particular wavelength can also be extracted, which can be imagined as taking a vertical cross section of the graph in Fig. 3.5. The intensity ratio of p- and s-polarized light on the grating against the angle of incidence at 750 nm is plotted in Fig. 3.6. The minimum measured is at 37° , while the theoretical resonance angle is calculated to be 33.1° using Eq. (2.9). The general shape of the reflectance around the trough consists of a small peak followed by a sharp drop to a minimum as the angle increases, and a more gradual rise after the minimum. Glancing at the graph, it is comparable to a similar graph of relative reflection intensity due to SPP excitation by Raether [11]. We are confident that the SPP resonance exists at the minimum reflection angle from the plot ($\theta \approx 37^\circ$).

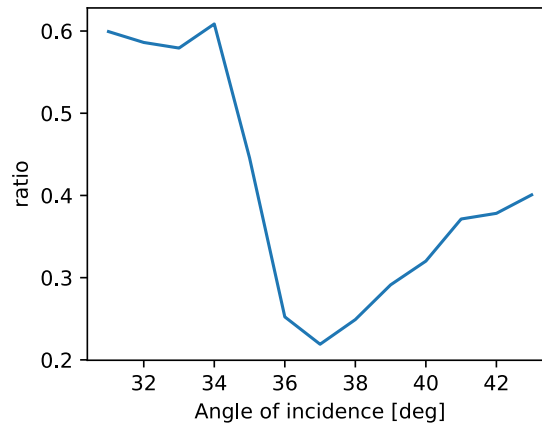


Figure 3.6: Intensity of the reflection at the grating as a ratio between p- and s-polarized light against the angle of incidence at 750 nm. The minimum suggests absorption caused by SPP excitation.

Calculating the resonance angle via Eq. (2.8) yields 33.1° . (Using the values $n = 1.958$ and $k = 7.571$ for the dielectric function of aluminium for light of 750 nm wavelength, from Ref. [13].) This discrepancy between the calculated value and the measured angle 37° could have originated from a number of factors. There could be an error in the measurement of the angles of incidence, since the white light is aligned by naked eye. The rotational mount holding the sample is rather crude, with markings at 2° intervals. The calculation of the angle θ from Eq. (2.9) is also an approximation in the first place. It is derived assuming a flat metal-dielectric interface, and the grating k-vector is simply added or subtracted to the wave vector of the incident light. This assumption is only valid if the amplitude of the grating is low. Furthermore,

the optical properties of the aluminium on our sample might be different from the literature values used.

3.5. Transient grating

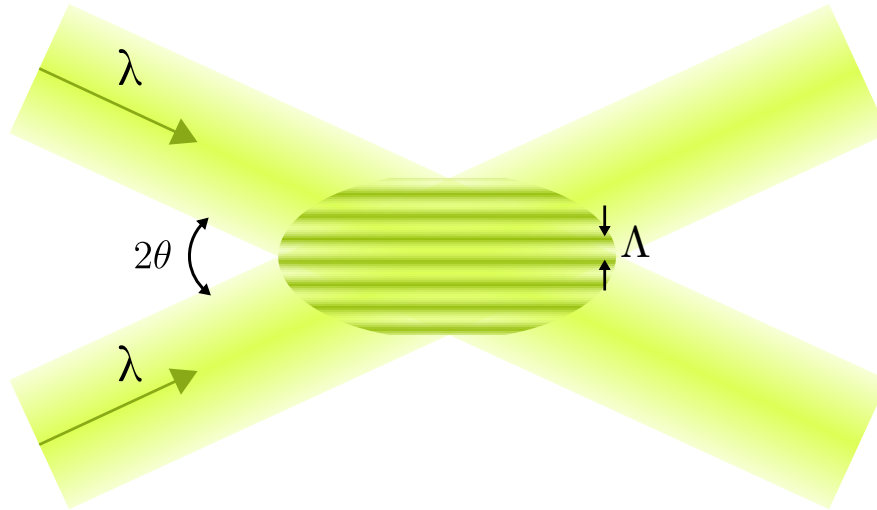


Figure 3.7: Schematic illustration of a transient grating formed by two intersecting laser beams.

In the first experiments, diffraction changes are measured using a transient grating to measure pump-induced optical changes and observing strain-wave-induced diffraction changes. When the path of two laser beams cross at an angle, and the two pulses arrive at the intersection at the same time, the electromagnetic fields create a spatial interference pattern at the intersection. If the two laser beams are incident onto the surface where the beam spots overlap, that area would experience alternating bright and dark fringes. Given that these laser pulses heat up and change the optical properties of the surface, these changes are also modulated by the interference pattern, creating a grating that diffracts light.

In our experimental setup, the 400 nm pump laser is split into two beams. They are both guided to be incident onto the sample where they overlap, forming the transient grating. A simple schematic of the geometry of two intersecting laser beams of the same wavelength is shown in Fig. 3.7.

By examining the geometry, we find that the periodicity Λ of the transient grating is given by,

$$\Lambda = \frac{\lambda}{2 \sin \theta} \quad (3.5)$$

where λ is the wavelength of the lasers and θ is the half angle between the two beams. By changing the angles of incidence and selecting the wavelength of the pump laser, the periodicity of the transient grating can be controlled. The relative phase between the two laser beam arms arriving at the sample surface would also affect the phase of the transient grating.

Also, the use of ultrafast lasers means that the time window in which the pulses from the two arms can actually intersect and interfere is short. The path difference leading to time delay between two pulses also requires adjustment such that they overlap temporally, and diffraction occurs.

The transient grating diffraction experiment is done on the flat part of the aluminium sample. Since a transient grating only exists when the pump laser pulses are present, diffraction only occurs for the pumped shot on a flat surface. The detector positioned to detect the diffracted light would detect nothing except scattered light for the blocked shot. In contrast, the reflection of the probe light always exists. The presence of a transient grating simply decreases the intensity of the reflection by a relatively small proportion. The transient grating measurements are in principle background-free, meaning no light should be measured if there is no transient grating pump on the sample. However, if the transient grating pump damages the sample, the probe light still diffracts when there is no pump, as the damage will typically only occur on the high-intensity fringes of the transient grating, meaning that the damaged spots will also be periodic with the same period as the transient grating pump. Calculating the relative change in diffraction would also be meaningless, as the diffraction signal without pump should be zero. Instead, the absolute change in diffraction is used.

Thus, we expect a higher signal-to-noise ratio in the transient grating diffraction change measurements than in reflection change measurements. The nearly zero signal from blocked shots also makes it unsuitable as a basis for the calculation of relative changes. Fluctuations near zero would cause arbitrary spikes in the relative changes, obscuring the actual diffraction change in a graph. The absolute difference is used instead to circumvent this distortion.

4

Results

4.1. Overview

In this chapter, we discuss the results of the pump-probe experiments carried out in this study. First, we discuss results from the transient grating diffraction change measurements. Second, we show reflection change measurements performed on the engraved grating using probe laser pulses of a narrow-band wavelength of 750 nm on a range of angles of incidence around the SPP resonance angle. Third, we show reflection change measurements on the grating using laser-generated white light continuum pulses incident at the SPP resonance angle for the wavelength of 750 nm on the grating sample. Finally, we discuss the acoustic impedance mismatch between the surface and the substrate material, in this case, aluminium and silicon, which is a major factor affecting the reflection of laser-induced longitudinal acoustic waves back to the surface.

4.2. Transient grating diffraction changes

In figures 4.1 (a) and (b), we plot the absolute measured pump-induced diffraction change as a function of the time delay between the pump and the probe, for two different pump/probe pulse energy values. The diameter of the pump beam spot on the sample is 4 times that of the probe beam spot. The diffraction change is also maximized by adjusting the positions of the beam spots to ensure that the probe

pulses are incident on the center of the excited transient grating. Each graph plots 3 traces measured in succession. The time delays are scanned in a zigzag way, from -20 ps to 100 ps in scan 1, with decreasing delays from 100 ps to -20 ps in scan 2 and again in ascending order in scan 3. Two measurements are performed using (a) a pump pulse energy of 25 μJ with a peak fluence of $8.55 \times 10^{-2} \text{ J/cm}^2$ and a probe pulse energy at 0.08 μJ with a peak fluence of $1.88 \times 10^{-3} \text{ J/cm}^2$, and (b) a pump pulse energy of 4 μJ with a peak fluence of $1.36 \times 10^{-2} \text{ J/cm}^2$ and probe pulse energy at 0.26 μJ with a peak fluence of $6.10 \times 10^{-3} \text{ J/cm}^2$. The calculation of the laser peak fluence is explained in appendix A.

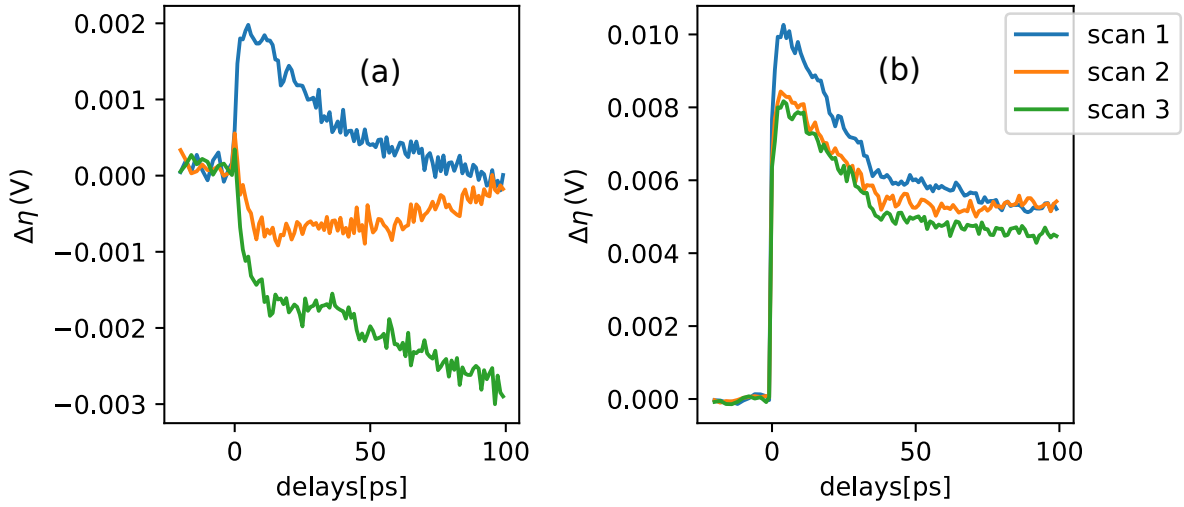


Figure 4.1: Transient grating first-order diffraction changes measured as a function of pump-probe delay for 750 nm probe wavelength with (a) pump pulse peak fluence of $8.55 \times 10^{-2} \text{ J/cm}^2$ and a probe pulse peak fluence of $1.88 \times 10^{-3} \text{ J/cm}^2$, (b) pump pulse peak fluence of $1.36 \times 10^{-2} \text{ J/cm}^2$ and a probe pulse peak fluence of $6.10 \times 10^{-3} \text{ J/cm}^2$.

For scan 1 in both (a) and (b), the diffraction efficiency is zero before the arrival of the pump pulse when $t < 0$ ps. Near $t = 0$ ps, we measure a sharp peak of diffraction increase. This is caused by electron dynamics where the electron gas rapidly absorbs the laser pulse energy and rises in temperature, changing the optical properties. Afterwards, the diffraction change decays as the energy in the electron gas is transferred to the lattice, while the energy also diffuses deeper into the material.

However, consecutive scans performed within the same measurement on the same spot result in different time-dependent diffraction changes; as seen in Fig. 4.1 (a), scan 2, when the time delay decreases, rather than showing roughly the same behaviour as

the first scan, the diffraction changes decrease immediately further into negative. The negative diffraction changes result from the detection of diffraction in the *blocked* shots, which did not exist at the start of the experiment. The longer the full measurement takes, the more the diffraction changes decrease across time delays, and it does not recover after a period of time without incident lasers pulses. This shows permanent changes in the sample surface after short periods of exposure to the laser light pulses, possibly damage to the surface, causing a grating to be imprinted permanently.

In light of the possible permanent damage, a new position of the sample is used for every new measurement. In Fig. 4.1 (b), we used a reduced pump pulse energy in an attempt to avoid or minimise permanent changes to the sample. To keep the signal strength high as the pump power decreases, we increased the probe pulse energy. The reduction in absolute diffraction changes across as the measurement progresses is smaller, yet still significant. Making conclusive observations of acoustic waves from such readouts is difficult since there exists permanent changes to the sample which we are unable to isolate from periodic signals caused by acoustic waves. More combinations of pump and probe pulse energies are used subsequently, yet we did not obtain clear and stable results. The lower the energies, the less permanent changes occur, but the absolute diffraction changes would also become too weak and inconsistent, with a very low signal-to-noise ratio.

As the transient grating excites the surface layer of the aluminium, the bright and dark fringes rapidly heat up the lattice in the same pattern. The thermal expansion of the lattice would generate longitudinal acoustic waves in the shape of the grating pattern. They propagate deeper into the aluminium layer, reflect off the silicon substrate and propagate back up to the surface. Therefore, we expect diffraction changes due to the reflected strain wave. The longitudinal speed of sound of aluminium is $v_l = 6420 \text{ m s}^{-1}$ [14], and the thickness of the aluminium layer is $d = 130 \text{ nm}$. The round-trip time for a longitudinal wave would be $T = 2d/v_l = 40.5 \text{ ps}$, and the corresponding frequency would be $f = 1/T = 24.7 \text{ GHz}$. Looking at the graphs, existence of echoes is unclear. There are some features in the traces near $t = 40 \text{ ps}$, which might be evidence of an echo, but we cannot draw strong conclusions.

4.3. Grating reflection changes

In this section, we discuss pump-probe reflection change measurements on the sample grating with a single pump laser pulse. Firstly, we measure reflection changes using probe pulses with a wavelength of 750 nm. This is performed at multiple angles at and around the SPP resonance angle. Then, we measure reflection changes using white light probe pulses at the resonance angle for 750 nm light, with a spectrometer. In all the measurements below, the laser peak fluence is controlled to a level that the reflectance does not change after prolonged exposure to the pump pulses during measurements. The relative reflection intensity at several angles of incidence is measured before each experiment to locate the SPP resonance angle of the sample.

4.3.1. Single wavelength probe

In Fig. 4.2, we plot the time-dependent reflectance changes for 750 nm probe light for pump-probe delays from $t = -10$ ps to $t = 1000$ ps. The probe pulse energy is 1.36 nJ whereas the pump pulse energy is 10 μ J. The pump pulse peak fluence is 60 J m⁻². We measure a spike of reflection decrease within the first 2 ps. Then the reflection change trace shows oscillations while decaying to near zero. In particular, from the graph, there are apparently two relatively strong valleys separated by approximately 420 ps. They are shear waves where the direction of displacement of the lattice is normal to the propagation of the waves, which is perpendicular to the grating lines. The wavelength of the dominant surface wave would inherit the period of the surface structure [2]. The period of our sample grating is 1600 nm and the transverse speed of sound v_t of aluminium is 3040 m s⁻¹ [14]. The predicted period of oscillations due to surface acoustic waves is calculated to be $T = \Lambda/v_t = 526$ ps. It is possible that the valleys separated by 420 ps are from the SAWs. There also appear to be more complex oscillations at higher frequencies, but we did not find the origin of these oscillations.

In order to more clearly observe oscillations of high frequencies, we proceed to perform measurements at shorter time delay intervals. The maximum time delay measured is reduced to 500 ps, allowing us to perform more measurements per day in the laboratory.

In Fig. 4.3, we plot multiple measurement runs performed in separate days at the SPP resonance angle. The general shapes of these measurements resemble the first 500 ps

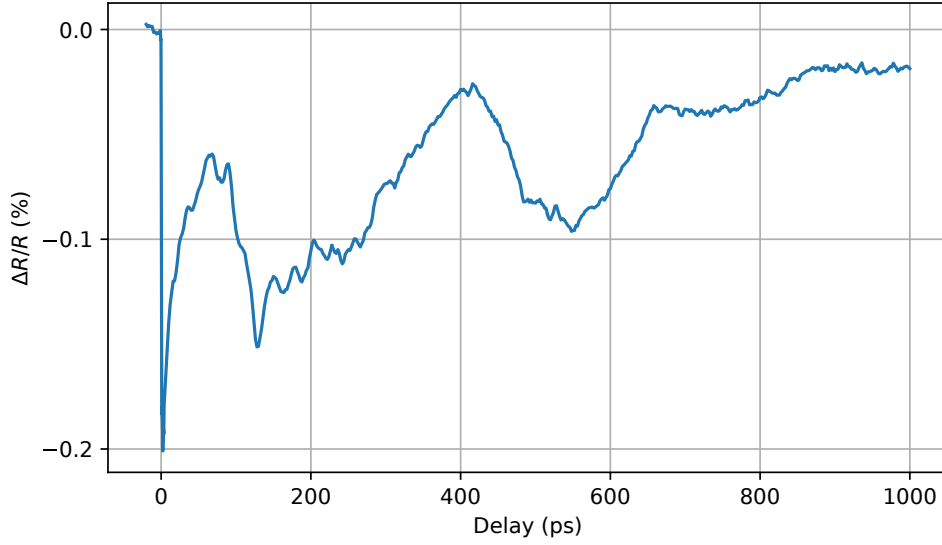


Figure 4.2: 750 nm wavelength probe pulse reflection changes measured as a function of time delay between pump and probe pulses excited by a single 400 nm pump beam, with the probe beam incident at the SPP resonance angle. The trace shown is the average of several scans.

of the measurement plotted in Fig. 4.2. The oscillation at a period of around 400 ps, and features such as the sharp valley at around $t = 130$ ps are consistently measured. However, we observe that different measurement runs exhibit significant variations when the measurements are separated by extended periods of time. There could also be inconsistencies in the position and angle of the sample and the signal detector since they have to be readjusted for misalignment every day. It is apparent that the signal strength and features measured in the time-dependent reflection changes are highly sensitive to the pump power and angle of incidence near the SPP resonance angle. Comparing the measurements taken on different days proves to be problematic due to the difficulty in alignment of the setup.

To ensure the comparability of separate measurements, we perform a series of measurements in a predefined set of angles in succession over the course of a single day. This minimises extra variations due to inconsistencies in the alignment and measurement of incident angles.

In Fig. 4.4, we plot pump-induced reflection changes with the probe beam incident at angles from -1° to $+1^\circ$ relative to the SPP resonance angle θ_{res} . We measure that the initial rapid decrease in reflection becomes weaker as the angle of incidence moves away from the SPP resonance angle. Surprisingly, as the angle of incidence gets smaller, the reflection changes move significantly towards the positive. At an

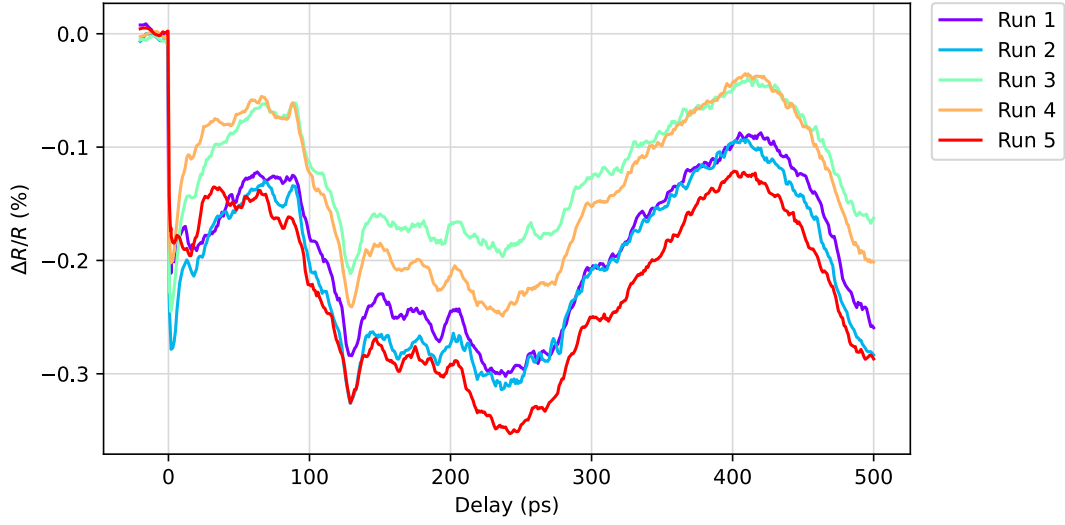


Figure 4.3: Pump-induced reflection changes with 750 nm wavelength probe pulses measured as a function of pump-probe time delay. The probe beam is incident at the SPP resonance angle. The five runs shown were measured in separate days.

incident angle only 0.25° smaller than θ_{res} , the reflection change offset caused by the heating of the aluminium is significantly smaller, on average by 0.1%, which is almost half the absolute value of the mean at θ_{res} . At -0.5° , the initial instantaneous spike turns positive, and the reflection changes oscillate between positive and negative. At -1° , the whole reflection change trace from $t = 0$ ps to $t = 500$ ps increases into the positive.

At angles larger than θ_{res} , the reflection changes also appear to move in the positive direction as the angle of incidence increases, to a lesser extent than reducing the angle. It is evident that the amplitude of the reflection change signal is not only sensitive to the angle of incidence, but the sign also changes depending on the angle.

To further investigate the behaviour of reflection change signals at off-resonance angles, more measurements are performed with a wider range of angles. In Fig. 4.5, we plot reflection changes with the probe beam incident at angles from -3° to $+3^\circ$ relative to θ_{res} . We observe a similar trend of reflection changes moving from the strongest negative changes at θ_{res} towards positive as the angle changes further from resonance. The average of the reflection changes moves in the positive direction more quickly when the angle is smaller than θ_{res} than when the angle is larger than θ_{res} . It appears that the evolution of the reflection change traces at angles smaller than θ_{res} is distinct from moving towards larger angles. We measure oscillations in the reflection change traces at angles at or smaller than θ_{res} with a period of around 110 ps.

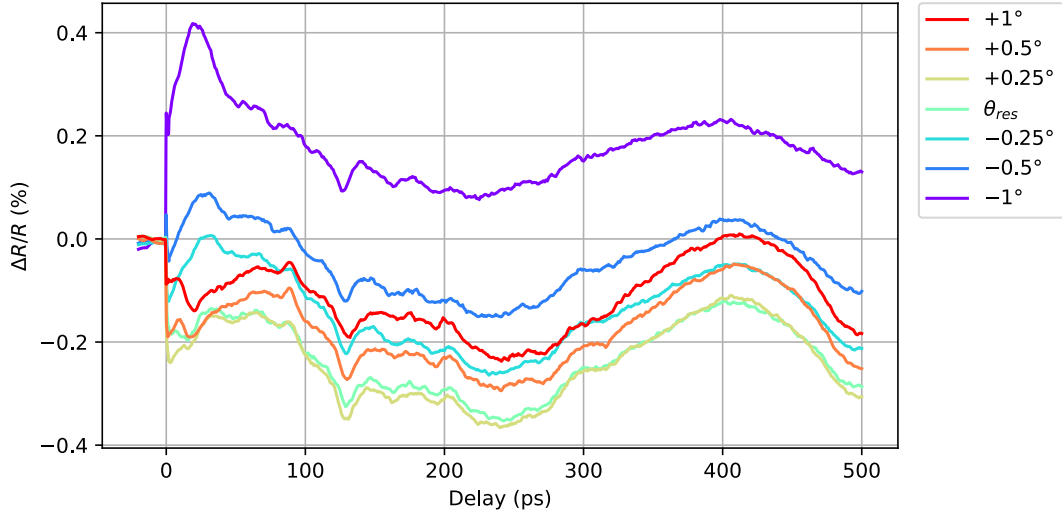


Figure 4.4: 750 nm wavelength probe pulse reflection changes as a function of pump-probe time delay, with the probe beam incident at angles from -1° to $+1^\circ$ relative to the SPP resonance angle θ_{res} .

To observe the evolution of the oscillations more clearly as the angle of incident changes, we plot the traces with each of their mean values averaged over the measurement time period subtracted in Fig. 4.6. We see that the major oscillations fade as the angle of incidence decreases from θ_{res} . Curiously, the amplitudes of the oscillations at angles larger than θ_{res} do not seem to shrink as the angle moves off-resonance even though the absolute value of the average reflection changes decreases. On the other hand, the oscillations shrink as the angle decreases and almost entirely disappear at -2° .

To discern the oscillation frequencies, the numerical fast Fourier Transform (FFT) is used on the time-dependent measurements to extract the amplitudes of oscillations in the frequency space. In Fig. 4.7 (a), we show the time-dependent probe pulse reflection changes, where measurement at each angle relative to the SPP resonance angle is given an offset for better visibility. The FFT of the time-dependent signals are shown in Fig. 4.7 (b) corresponding to each angle of incidence.

In Fig. 4.7 (b), starting from the angle of incidence at θ_{res} , a peak is measured near 9 GHz. This peak also exists as the angle increases from θ_{res} to $+3^\circ$. These peaks correspond to the oscillations with a period of ~ 110 ps we see in the time-dependent reflection change plots from θ_{res} to $+3^\circ$. At angles of incidence from -1° to -3° , smaller than θ_{res} , the FFT curves show a steep initial rise followed by a gradual

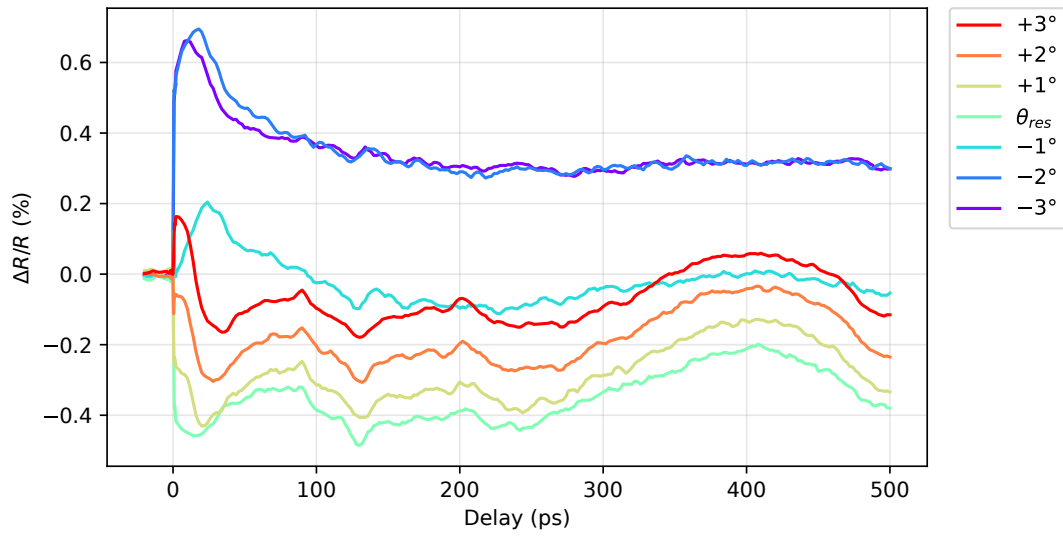


Figure 4.5: 750 nm wavelength probe pulse reflection changes as a function of pump-probe time delay, with the probe beam incident at angles from -3° to $+3^\circ$ relative to the SPP resonance angle θ_{res} .

decay from low to high frequencies, without any prominent oscillation frequency to be found. This reflects the fact that the time-domain signal is similar to a simple exponential decay without any prominent periodic oscillation.

From these results, we do not find clear indication of oscillations due to longitudinal waves reflecting off the substrate as expected, which are predicted to be at 24.7 GHz. Regarding the 9 GHz oscillations measured at the angles of incidence from θ_{res} to $+3^\circ$, we are yet to identify the mode of the underlying acoustic waves.

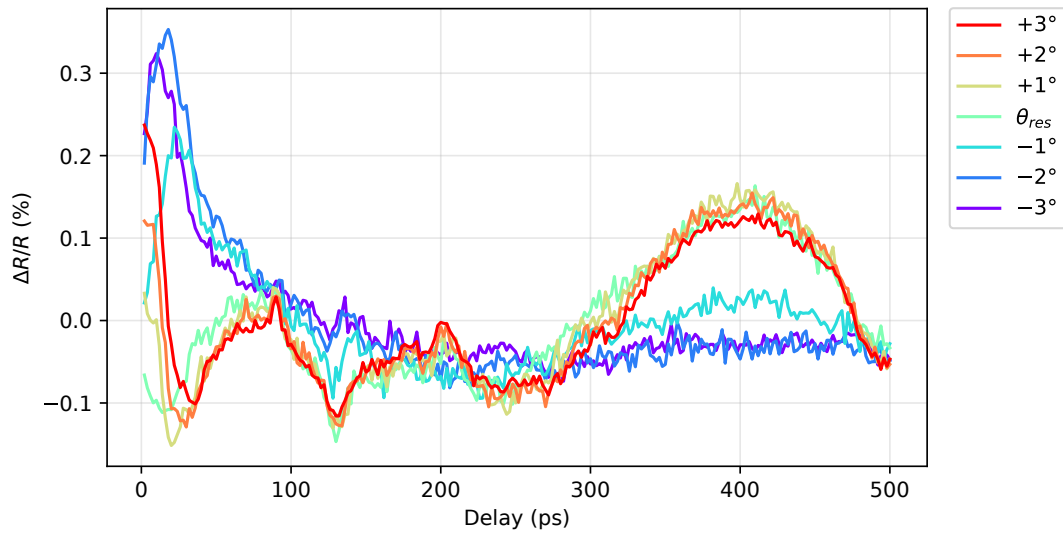


Figure 4.6: Probe pulse reflection changes as a function of pump-probe time delay, with the probe beam incident at angles from -3° to $+3^\circ$ relative to the SPP resonance angle θ_{res} . The mean of the traces at each angle is subtracted.

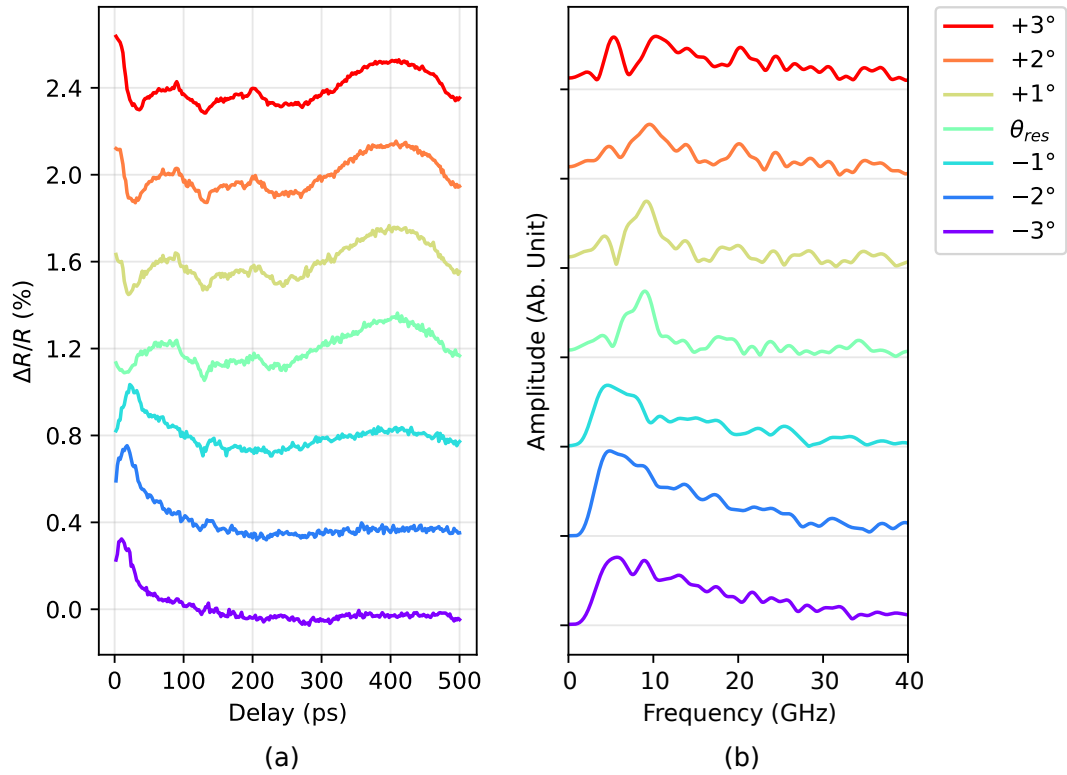


Figure 4.7: (a) Probe pulse reflection changes as a function of pump-probe time delay, with the probe beam incident at angles from -3° to $+3^\circ$ relative to the SPP resonance angle θ_{res} . The mean of the traces at each angle is offset for better visibility. (b) FFT of the time-dependent reflection changes signals for each corresponding angle.

4.3.2. White light probe

In Fig. 4.8, we plot the measured pump-induced reflection changes as a function of both the time delay between the pump and probe pulses and the probe wavelength. The relative reflection changes are represented by color. The probe pulses are incident at the SPP resonance angle for wavelength 750 nm. The reflection changes are the mean of 4 measurement scans across time delays from -20 to 500 ps. From the plot, we observe that the reflection changes at most time delays at θ_{res} are only positive at wavelengths near 750 nm. For the probe wavelengths longer than around 780 nm or lower than around 740 nm, the reflection changes transition to positive. There is also a band of negative reflection changes around the wavelength of 880 nm. This matches the minimum in the reflection ratio spectrum at 880 nm. There is a minimum feature at around 130 ps across the spectrum we measured, which was also measured in the angle-dependent measurements in the previous experiment. However, due to the reflection change contrast across different wavelengths, it is difficult to discern the time-dependent oscillations at each wavelength.

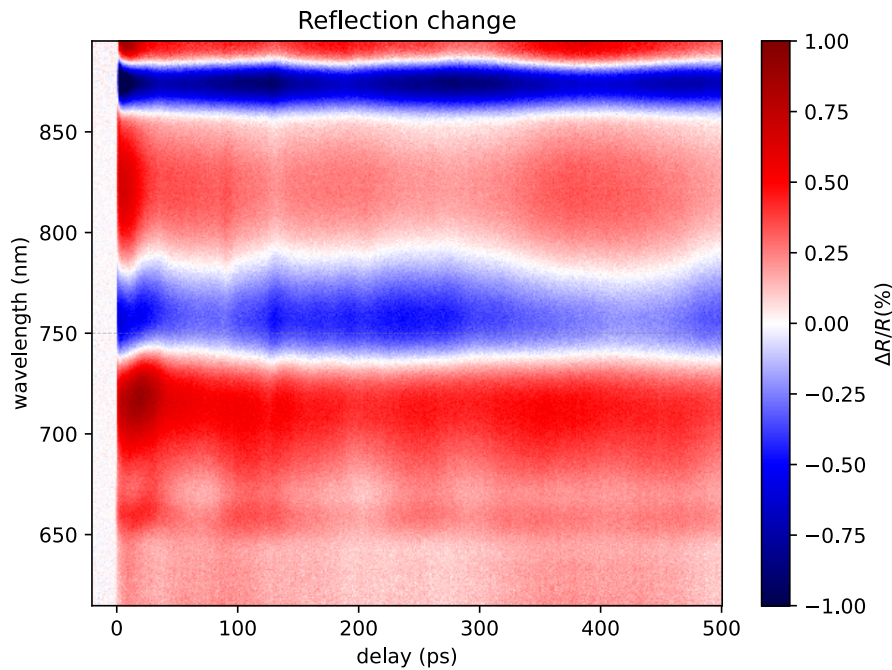


Figure 4.8: Pump-induced reflection changes as a function of the time delay between the pump and probe pulses on the x-axis, and the wavelength on the y-axis. The relative reflection changes are represented by a color scale from -1% to +1%, where white represents 0%. The probe pulses are incident at the SPP resonance angle for wavelength 750 nm.

To make discerning the time-dependent oscillations easier, we subtract from the reflection change measurement the mean over the whole measurement time period. FFT of the time-dependent measurements is also calculated to analyze the oscillation frequencies. In Fig. 4.9 (a), we plot the reflection changes with the mean subtracted, and in (b) the FFT with respect to time. We also plot the reflection changes with a 4 GHz high-pass filter in (c), and the corresponding FFT plot in (d).

In Fig. 4.9 (a), the existence of periodic oscillations is still not obvious when looking at the time-dependent measurements. We observe a minimum feature at around $t = 130$ ps, which is measured consistently at all wavelengths in the measured spectrum. In 4.9 (b), prominent oscillation frequencies are also not clearly observed. Despite the weak amplitudes of the frequencies, we see that the amplitudes of most frequencies seem to be weaker around the resonance frequency at 750 nm. As acoustic waves involving the modulation of material density cause the resonance frequency to oscillate, their reflection change signals peak at the *slopes around* the SPP resonance wavelength, but the magnitude decreases at the resonance [2]. This could be an evidence of the existence of higher frequencies density modulating waves. However, it is difficult to draw any conclusion from due to their relatively weak signal.

By processing the reflection change signal through a high-pass filter, which attenuates signals with frequencies lower than the cutoff, oscillations at higher frequencies can be revealed. The low frequencies of around 2 GHz are close to the predicted frequency caused by surface acoustic waves, and the corresponding period is approximately equal to the whole measurement time window of 500 ps. The high-pass filters eliminates these frequencies from the FFT plot.

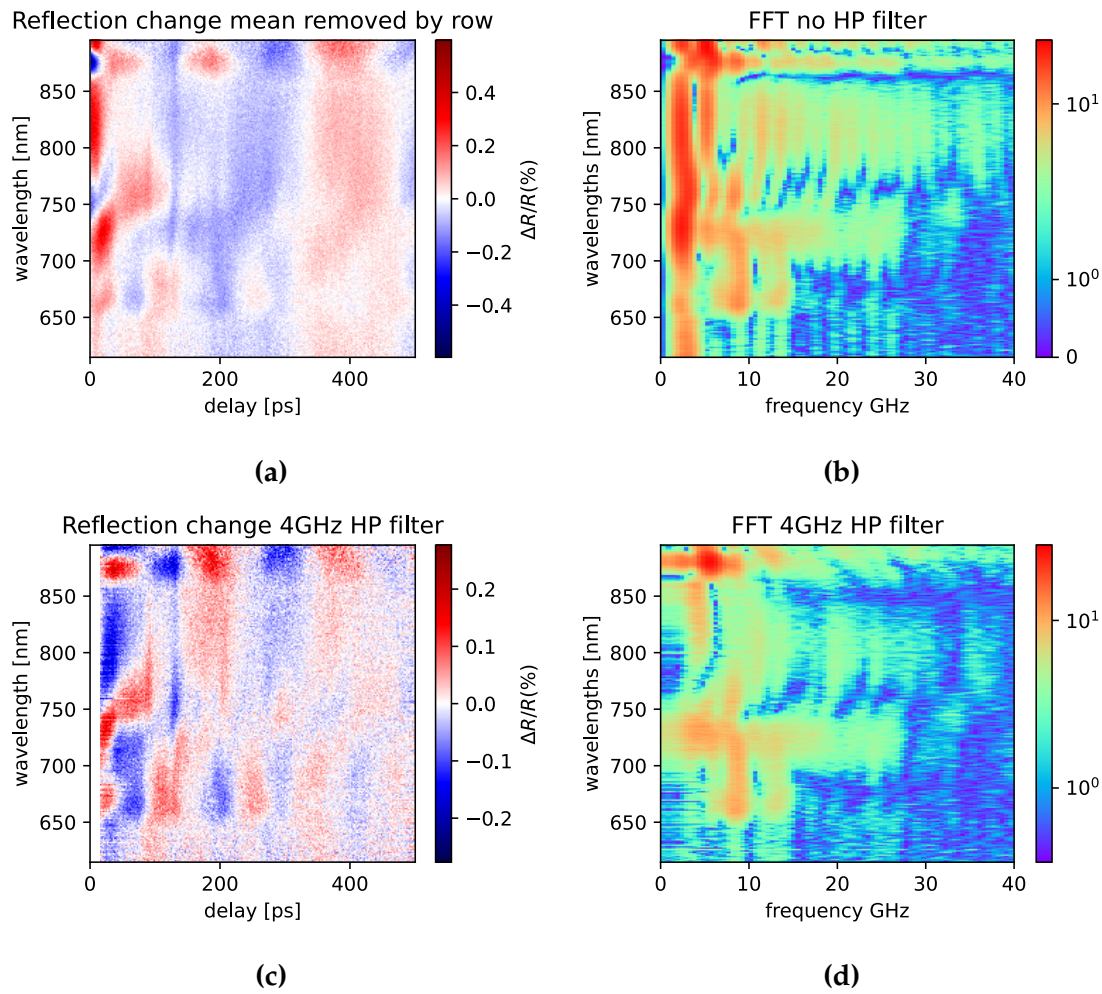


Figure 4.9: Pump-induced reflection changes measured with probe incident at θ_{res} for 750 nm wavelength, as a function of the time delay between the pump and probe pulses on the x-axis and the wavelength on the y-axis, represented by a color scale. The mean is subtracted for each wavelength (a) with no filter, and (c) with a 4 GHz high-pass filter. FFT of the reflection change measurements (b) with no filter, (d) with 4 GHz high-pass filter. The color scales in the time-dependent graphs are scaled to maximize contrast and the color scales in the FFT graphs are logarithmic.

In Fig. 4.9 (c), the reflection change signal is filtered at a high-pass cutoff of 4 GHz. We observe more clearly the prominent frequencies around 9 GHz, at the probe wavelengths from around 650 nm to 770 nm. At wavelengths above 750 nm, the strength of the frequencies around 9 GHz decreases as the wavelength increases. However, we still do not observe clear periodic oscillations with a 40.5 ps period corresponding to the 24.7 GHz longitudinal wave echoes. From the FFT as well, there

is no significant peak around 24.7 GHz to indicate the presence of strong longitudinal wave echoes.

Some similarities are observed between the white light probe measurement and the angle-dependent 750 nm wavelength probe measurements. If we compare the time-dependent measurements in Fig. 4.9 (a, c) with the 750 nm wavelength probe measurements shown in Fig. 4.7 (a), we see the same minimum feature at about $t = 130$ ps measured across changing angles at 750 nm, and across the spectrum measured at a fixed angle in the white light probe measurements. In addition, the 9 GHz oscillations measured at fixed probe wavelength of 750 nm at angles of incidence from 0° to 3° larger than the SPP resonance angle, plotted in Fig. 4.7, are also measured in the white light probe measurements between 650 and 770 nm probe wavelengths, shown in Fig. 4.9 (d). However, the nature of these features and oscillations are still unknown. We speculate that the 9 GHz oscillations can be the grating line quasi-normal modes, which were measured in a previous study by de Haan et. al. [6] of a similar sample with gold deposited on a SiO_x grating. However, we are unable to attribute frequencies to such modes in our own sample.

In Fig. 4.10, we plot the probe pulse reflection changes, (a) from the 750 nm probe wavelength measurement with the probe beam incident at angles from -3° to $+3^\circ$ relative to the SPP resonance angle θ_{res} (original data without offset is plotted in Fig. 4.5), and (b) from the white light probe measurement incident at the θ_{res} with the probe wavelengths from 720 to 780 nm extracted from the spectrum. We see that measuring at increasing angles of incidence and measuring at increasing probe wavelengths show similar effects on the reflection changes. For instance, in the larger angles of incidence and with the longer probe wavelengths, the initial peak near $t = 20$ ps drops into the negative, the minimum near $t = 130$ ps becomes increasingly negative, and the maximum around $t = 400$ ps becomes more prominent.

To understand the relation between the angle of incidence and the incident wavelength around the SPP resonance conditions, we consider the SPP resonance conditions from Eq. (2.9). Light can only be coupled to an SPP on a metal grating if the x-component of the wave vector k_x of the incident light satisfies the equality for our grating with a fixed k_g . In our case, we consider $N = 1$. The incident light can excite an SPP if

$$k_x = \frac{\omega}{c} \sin \theta = k_{SPP} - k_g, \quad (4.1)$$

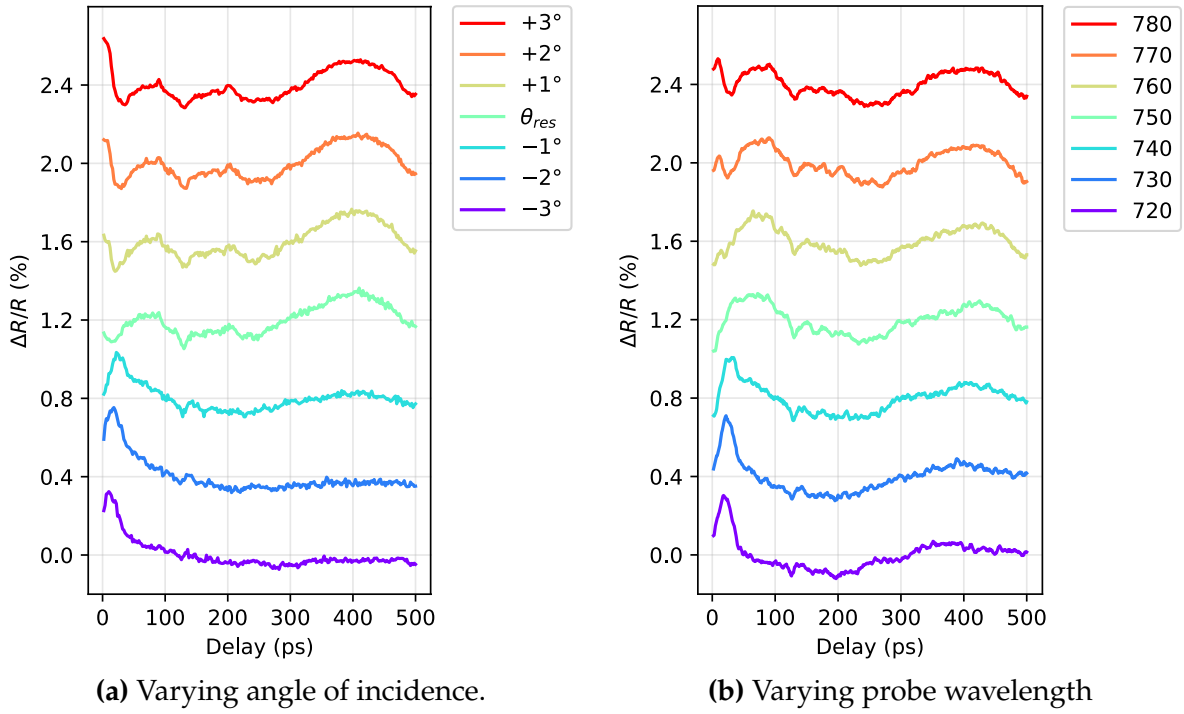


Figure 4.10: Probe pulse reflection changes, (a) from the 750 nm probe wavelength measurement with the probe beam incident at angles from -3° to $+3^\circ$ relative to the SPP resonance angle θ_{res} , and (b) from the white light probe measurement incident at the θ_{res} with the probe wavelengths from 720 to 780 nm.

where $k_g = 2\pi/\Lambda$, which is a constant, where Λ is the grating period, and k_{SPP} depends on the dielectric function of the metal, which is a function of the wavelength of light. Using the dielectric function of aluminium from Ref. [13] and the grating period of 1600 nm on our sample, we calculate the SPP resonance wavelength as a function of the angle of incidence. The result is plotted in Fig. 4.11.

As the angle of incidence increases, the SPP resonance wavelength decreases. This is a result of the dispersion relation of k_{SPP} with respect to the frequency of light shown in Fig. 2.2. k_{SPP} grows faster than the k-vector of the incident light $k_0 = \omega/c$ for increasing frequency of light. Given a fixed k_g , the higher the frequency, or the shorter the wavelength, the larger k_x is required to satisfy the sum $k_{SPP} = k_x + k_g$. This relation also means that, by slightly increasing the angle of incidence from resonance, the incident light would become off-resonance on the longer wavelength side of the SPP resonance valley in the reflectance spectrum, and vice versa on the shorter wavelength side of the resonance.

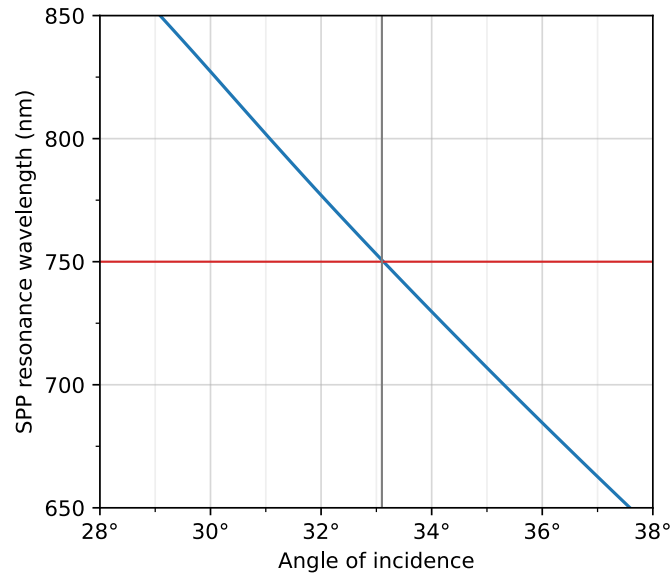


Figure 4.11: SPP resonance wavelength against angle of incidence. Values are calculated for an aluminium grating sample with a grating period of 1600 nm, using Eq. 2.9, with $\epsilon_d = 1$ and dielectric function ϵ_m of aluminium given by Ref. [13]. Vertical grey line indicates the calculated SPP resonance angle at 33.1° for the wavelength of 750 nm.

A schematic representation of the reflectance spectrum in the vicinity of the minimum around the SPP resonance is shown in Fig. 4.12. The wavelength λ_{res} at resonance at the angle of incidence θ_{res} would be on the slope of the resonance valley when the angle of incidence changes. Therefore, it is likely that increasing the angle of incidence at a constant probe wavelength produce similar effects as increasing the probe wavelength while keeping the angle of incidence constant as they both result in probing on the slope of the resonance. This could be a possible reason for the similarity between Fig. 4.10 (a) and (b).

The signals from longitudinal wave oscillations are reported to be amplified at the slope of the SPP resonance since the compression of the material decreases SPP resonance wavelength while expansion increases SPP resonance wavelength [6]. Their signal can potentially be amplified by using off-resonance angles of incidence using a fixed probe wavelength. These are under the assumption that the effect of the pump laser on the dielectric function of the sample is homogeneous across different wavelengths of light, and that the general shape of the valley around the SPP resonance wavelength in the reflectance spectrum does not change significantly when

the resonance wavelength changes. In our case, the assumptions apply since the real part of the dielectric function of aluminium in the wavelength range of 700–800 nm show little variation [15].

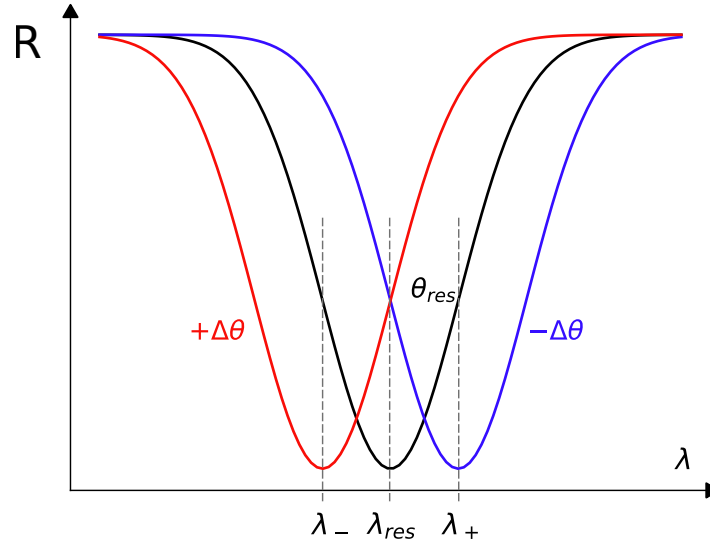


Figure 4.12: Schematic representation of the reflectance spectrum in the vicinity of the minimum around the SPP resonance. A small change to the angle of incidence θ causes the SPP resonance wavelength to change accordingly.

In all of our experiments, the anticipated longitudinal wave echoes are not clearly measured. Moreover, as shown in Fig. 4.8, the reflection change signals change sign at off-resonance wavelengths. Thus, it is unclear how the acoustic wave signals can be enhanced with SPP resonance. Also, the sources of the features and oscillations measured remain unknown.

One of the potential reasons we did not measure the longitudinal waves is the quality of the aluminium deposition. The aluminium layer deposited may be porous, dampening the propagation of waves. Another reason may be the lack of acoustic impedance mismatch between aluminium and the silicon substrate, which is discussed in the following section.

4.4. Acoustic impedance mismatch

To get longitudinal wave echoes, acoustic impedance mismatch between the sample metal aluminium and the silicon substrate is required for the reflection of acoustic waves from their interface back to the surface.

Acoustic impedance is a physical property of a material that describes the resistance to acoustic waves transmitting through. The acoustic impedance Z of a medium is defined as the product of the density ρ of the material and the speed of sound v in that material [16].

$$Z = \rho v \quad (4.2)$$

It is an important parameter that determines how much a sound wave is reflected and transmitted at an interface between two media. The fraction of the amplitude of the sound wave reflected at the boundary is defined as the reflection coefficient R . It is determined by

$$r = \sqrt{\frac{I_r}{I_i}} = \left| \frac{Z_1 - Z_2}{Z_1 + Z_2} \right|, \quad (4.3)$$

where I_r and I_i are the intensities of the reflected and incident sound wave, Z_1 and Z_2 are the acoustic impedance of the two media. From this equation, the more similar the acoustic impedance of the two media, the less fraction of a sound wave can be reflected. The difference in acoustic impedance is referred to as the *acoustic impedance mismatch*.

Material	Al	Si	SiO ₂
Density ρ (kg m ⁻³)	2710	2330	2650
Speed of sound v (m s ⁻¹)	6420	8430	5780
Acoustic impedance Z (10 ⁶ kg s ⁻¹ m ⁻²)	17.4	19.6	15.4
Reflection coefficient r with Al	0%	5.95%	6.10%

Table 4.1: Acoustic properties for Al, Si and SiO₂. Densities and speeds of sound from Ref. [14].

Using the known values for the density and speed of sound for aluminium and silicon, their acoustic impedance values are calculated. They are shown in Table 4.1. The acoustic impedance mismatch between Al and Si is rather small. By Eq. (4.3), the reflection coefficient r between the aluminium and the silicon substrate

is calculated to be only approximately 6%. There may exist an oxide layer on the silicon wafer substrate under the aluminium, changing the reflection coefficient at the interface from which the pump-induced acoustic waves are reflected, though it is probably so thin that most of the acoustic wave is transmitted through. Assuming the layer between the aluminium and the silicon substrate consists of SiO_2 , the acoustic impedance mismatch between Al and SiO_2 is still small. The reflection coefficient r between Al and SiO_2 is calculated to be approximately 6%.

From these calculations, it is evident that only a very small fraction of the longitudinal wave propagating into the layer is reflected back to the aluminium surface. Even the first acoustic echo may be too difficult to detect by the probe laser. This is probably a major reason for the absence of clear signals for the laser-induced longitudinal waves.

In future studies of the detection of longitudinal wave reflections, the acoustic impedance mismatch should be taken into consideration when choosing the pair of materials forming the interface for reflection.

5

Conclusion

In this thesis, we studied ultrafast laser-induced photoacoustics on a thin aluminium layer deposited on a silicon wafer with a grating structure, using pump-probe experiments. Transient grating diffraction measurements and reflection change measurements at and around the surface plasmon polariton (SPP) resonance angle are employed.

The transient grating experiments showed unstable and noisy signals, complicating the observation of acoustic waves. It demonstrated that pump-induced diffraction changes were highly sensitive to the laser pulse energies. Results suggests damage to the sample surface when exposed to the pump pulses at higher the pump energies required in a transient grating measurement. Although we expected to observe longitudinal acoustic wave reflections corresponding to the round-trip time of waves in the aluminium layer, clear evidence of these echoes was not observed due to insufficient signal strength with a low damage threshold for the pump pulse energy.

In the experiments on the engraved grating using probe pulses at the wavelength of 750 nm, we measured reflection changes at several angles of incidence around the SPP resonance angle. Oscillations with a frequency around 9 GHz, and a minimum feature at around 130 ps delay were observed, but their origin remains unknown, suggesting the presence of acoustic phenomena more complex than initially expected.

In the experiments on the grating part using white light continuum pulses, we measured reflection changes in a spectrum of wavelengths from 600 to 900 nm,

incident at the SPP resonance angle for 750 nm. Oscillations with a frequency around 9 GHz are also observed for wavelengths of 650–770 nm, and the minimum feature at around 130 ps was also found across the spectrum. However, the expected 24.7 GHz oscillations due to longitudinal wave echoes are still not clearly measured. We studied the relation between increasing the angle of incidence around the SPP resonance and increasing the probe wavelength around the SPP resonance. It may explain the similarity of their effects on the features on time-dependent reflection change traces.

Without clear signals of photoacoustic waves, the enhancement of reflection changes signals of acoustic waves with SPP resonance remains inconclusive. The absence of longitudinal wave echoes in our measurements is likely due to insufficient acoustic impedance mismatch between the aluminium layer and the silicon substrate, which limits the reflection coefficient of acoustic waves at the interface between the aluminium and the silicon substrate.

References

- [1] C. De Guzman, "The smallest chip ever," *Time*, Nov. 2022.
- [2] G. de Haan, "Enhanced generation and detection of ultrafast laser-induced acoustic signals," *Thesis, fully internal, Universiteit van Amsterdam*, 2022.
- [3] E. Kretschmann and H. Raether, "Notizen: Radiative Decay of Non Radiative Surface Plasmons Excited by Light," en, *Zeitschrift für Naturforschung A*, vol. 23, no. 12, pp. 2135–2136, Dec. 1968, ISSN: 1865-7109, 0932-0784. DOI: 10.1515/zna-1968-1247.
- [4] R. Ritchie, E. Arakawa, J. Cowan, and R. Hamm, "Surface-Plasmon Resonance Effect in Grating Diffraction," en, *Physical Review Letters*, vol. 21, no. 22, pp. 1530–1533, Nov. 1968, ISSN: 0031-9007. DOI: 10.1103/PhysRevLett.21.1530.
- [5] N. Khokhlov, G. Knyazev, B. Glavin, Y. Shtykov, O. Romanov, and V. Belotelov, "Interaction of surface plasmon polaritons and acoustic waves inside an acoustic cavity," *Optics Letters*, vol. 42, no. 18, pp. 3558–3561, 2017.
- [6] G. d. Haan, V. Verrina, A. J. L. Adam, H. Zhang, and P. C. M. Planken, "Plasmonic enhancement of photoacoustic-induced reflection changes," EN, *Applied Optics*, vol. 60, no. 24, pp. 7304–7313, Aug. 2021, Publisher: Optica Publishing Group, ISSN: 2155-3165. DOI: 10.1364/AO.432659.
- [7] Anisimov, SI and Kapeliovich, BL and Perelman, TL and others, "Electron emission from metal surfaces exposed to ultrashort laser pulses," *Zh. Eksp. Teor. Fiz*, vol. 66, no. 2, pp. 375–377, 1974.
- [8] A. Nicarel, M. Oane, I. N. Mihailescu, and C. Ristoscu, "Fourier two-temperature model to describe ultrafast laser pulses interaction with metals: A novel mathematical technique," en, *Physics Letters A*, vol. 392, p. 127 155, Mar. 2021, ISSN: 03759601. DOI: 10.1016/j.physleta.2021.127155.
- [9] C. Thomsen, H. T. Grahn, H. J. Maris, and J. Tauc, "Surface generation and detection of phonons by picosecond light pulses," en, *Physical Review B*, vol. 34, no. 6, pp. 4129–4138, Sep. 1986, ISSN: 0163-1829. DOI: 10.1103/PhysRevB.34.4129.

- [10] M. Bonn, D. N. Denzler, S. Funk, M. Wolf, S.-S. Wellershoff, and J. Hohlfeld, "Ultrafast electron dynamics at metal surfaces: Competition between electron-phonon coupling and hot-electron transport," en, *Physical Review B*, vol. 61, no. 2, pp. 1101–1105, Jan. 2000, ISSN: 0163-1829, 1095-3795. DOI: 10.1103/PhysRevB.61.1101.
- [11] H. Raether, *Surface Plasmons on Smooth and Rough Surfaces and on Gratings* (Lecture Notes in Control and Information Sciences). Springer-Verlag, 1988, ISBN: 978-3-540-17363-2. [Online]. Available: <https://books.google.nl/books?id=ZLwrAAAAYAAJ>.
- [12] I. Epstein, I. Dolev, D. Bar-Lev, and A. Arie, "Plasmon-enhanced Bragg diffraction," en, *Physical Review B*, vol. 86, no. 20, p. 205 122, Nov. 2012, ISSN: 1098-0121, 1550-235X. DOI: 10.1103/PhysRevB.86.205122.
- [13] M. N. Polyanskiy, "Refractiveindex.info database of optical constants," en, *Scientific Data*, vol. 11, no. 1, p. 94, Jan. 2024, ISSN: 2052-4463. DOI: 10.1038/s41597-023-02898-2.
- [14] "CRC Handbook of Chemistry and Physics, 84th Edition Edited by David R. Lide (National Institute of Standards and Technology). CRC Press LLC: Boca Raton. 2003. 2616 pp. ISBN 0-8493-0484-9," *Journal of the American Chemical Society*, vol. 126, no. 5, 2004. DOI: 10.1021/ja0336372.
- [15] P. R. Wiecha, M.-M. Mennemanteuil, D. Khlopin, *et al.*, "Local field enhancement and thermoplasmonics in multimodal aluminum structures," en, *Physical Review B*, vol. 96, no. 3, p. 035 440, Jul. 2017, ISSN: 2469-9950, 2469-9969. DOI: 10.1103/PhysRevB.96.035440.
- [16] L. E. Kinsler, A. R. Frey, A. B. Coppens, and J. V. Sanders, Eds., *Fundamentals of acoustics*, 4th ed. New York: Wiley, 2000, ISBN: 978-0-471-84789-2.

A

First appendix

A.1. Laser peak fluence

In an ultrafast laser pump-probe experiment, we repeatedly pump the sample with a strong laser pulse and probe it afterwards with a probe laser pulse. Ideally, any optical changes induced by a pump pulse should completely dissipate before the next one such that the effects of pump shots do not accumulate. In order to avoid excessive energy inducing permanent changes or damage to the sample, it is important to keep track of the peak fluence of the pump and probe pulses in each measurement. Optimally, we would like to keep the pump-probe laser pulse energies as high as possible for the best signal strength, while avoiding damage. A peak fluence calculation is helpful for setting suitable laser power levels before measurement.

To calculate the laser fluence, we need to measure the spot size of the laser on the sample. By placing a beam profiler at the position of the sample, we measure the beam intensity distributions and they are approximately Gaussian. The full widths at half maximum (FWHM) intensity of the beam spots are measured. The beam spots in general are elliptic. The widths are given in the two axes, w_x and w_y of the ellipse drawn at the FWHM. The spot size at FWHM can be calculated as,

$$A = \pi ab = \pi w_x w_y / 4 \quad (\text{A.1})$$

We can also measure the power P of the beam incident on the sample. The peak

fluence of a Gaussian beam is then given by,

$$F_{peak} = \ln(2) * \frac{P}{A f_{shots}} \quad (\text{A.2})$$

f_{shots} is the frequency of shots. 500 Hz for the pump and 1000 Hz for the probe. For a transient grating, the peak fluence is higher than the fluence of the peaks of the two beams combined due to constructive interference at the bright fringes. In this case, the peak fluence is 4 times the peak fluence for a single beam with the same power as one beam in the transient grating.

Although the energy of the probe pulses is relatively low, it should still be added to the peak fluence in the calculation since its spot size is much smaller than the pump beam; thus, the probe pulse energy is more concentrated, making the peak fluence potentially comparable to the pump pulses. The peak fluence is the sum of the peak fluence of a probe pulse and a pump pulse. The probe pulse energy is less significant in the reflection change measurements, as lower powers are used. Reflectance in general is much higher than the diffraction efficiency of a transient grating, requiring lower energy probe pulses to collect enough light for a decent signal-to-noise ratio.